

IISc THESES ABSTRACTS

Thesis Abstract (Ph.D.)

Prebreakdown and breakdown phenomena in composite dielectrics with special reference to electronegative gases and their mixtures by S. V. Kulkarni.

Research supervisor: R. S. Nema.

Department: High Voltage Engineering.

1. Introduction

Out of a variety of gases used in insulation system, SF₆ is found to be of great importance due to its high dielectric strength. In addition, SF₆ has certain properties such as good thermal conductivity, arc-quenching ability, chemical inertness and stability, non-inflammability, non-toxicity compared to other gases used as insulation. However, SF₆ being an expensive gas with a low pressure of liquifaction and also the effect of free particles being high in SF₆, a good amount of research is being done on mixtures of electronegative gases with ordinary gases to overcome the above drawbacks and also to find better insulating gases. The aim of the work in this thesis is to correlate the breakdown voltage data in various gases and mixtures and to study the prebreakdown phenomena, partial discharge behaviour and breakdown in SF₆ and mixtures.

2. Main results and discussion

2.1. Unified approach to calculate breakdown voltages

In the design of insulation, breakdown voltages and corona inception voltages play a major role. A large amount of data is available in literature on breakdown and their mixtures. However, it is difficult to use these data because they are not formulated properly. The empirical, semiempirical and theoretical formulae for predicting breakdown voltages available in literature are either complicated or are valid under limited conditions. There is a need to coordinate these data in the form of a simple expression. Hence, by taking into consideration all the above points, efforts are made to develop a simple equation which applies to electronegative gases and mixtures under alternating and direct voltage conditions. The developed equation is valid under uniform and nonuniform field conditions by taking into account the field utilisation factor. The equation is shown to be valid for 15 gases and their mixtures under different conditions of pressure distance and electrode geometries for 1 to 100% of the main electronegative gas.

The developed equation has the form

$$V_{\text{mix}} = K_1 (Pd)^a \cdot \exp(K_2 N^b) \cdot U^c$$

where V_{mix} is the breakdown voltage of mixture, P the pressure of the gas, d the distance between electrodes, N the percentage of main electronegative gas, U the field utilisation factor and K_1 , a , K_2 , b , and c are constants.

An attempt is made to explain the physical basis of the developed equation. In order to understand further the physical basis of the developed equation, the behaviour of the Townsend's first ionisation coefficient is explained theoretically. It is observed that Townsend's equation of α/p gets modified in case of binary mixture in such a way that the equation of $(\alpha/p)_{\text{mix}}$ also shows a similar form like Townsend's α/p equation.

The equation obtained is

$$(\alpha/p)_{\text{mix}} = A^+ e^{-B^+ P \cdot E}$$

where

$$A^+ = \frac{A_1 PC_1 + A_2 PC_2}{PC_1 + PC_2}$$

and

$$B^+ = \frac{B_1 PC_1 + B_2 PC_2}{PC_1 + PC_2}$$

where, A_1 and B_1 are the constants for the first gas and A_2 and B_2 are the constants for the second gas. The measured values of $(\alpha/p)_{\text{mix}}$ available in literature agree well with the calculated values.

2.2. True shapes of corona and breakdown pulses

Experiments were conducted on breakdown of SF_6 and N_2 mixtures under uniform field conditions to confirm the versatility of the developed equation, to fill the gap in the literature. The effect of UV irradiation on breakdown is studied in depth and it was observed that there was a decrease in breakdown voltage in the presence of UV irradiation.

The results of the detection of true pulse shapes of prebreakdown and breakdown pulses are quite encouraging. The effect of circuit parameters, current-limiting resistance, UV irradiation, field nonuniformity, overvoltages, pressure and the distance between electrodes, gases and their mixtures are studied in depth. Most of the experiments are conducted using alternating voltages. In a few experiments the true shapes are studied using direct voltage conditions also. The main purpose of using alternating voltages is to understand the pulsating nature of the discharge. It is observed that the number of breakdown pulses depend on the operating point on the I-V characteristic and on the current-limiting resistance. The gases studied are air, N_2 , O_2 , CO_2 , SF_6 and $\text{SF}_6 + \text{N}_2$ mixtures. The experimental results are discussed in three parts *i.e.* under uniform, different (from uniform field to extremely nonuniform field conditions) and extremely nonuniform field conditions. Efforts are made to understand the reasons for shapes of prebreakdown and breakdown pulses. The results are discussed in terms of rise time, fall time, pulse magnitude, charge of the pulse and the number of pulses per cycle. The development of the discharge is studied from the current pulses under different conditions and relative study of gases is made. Many interesting results like pulsating nature of the discharge, effect of UV irradiation on area of the electrode, the behaviour of Trichel pulses in the presence of UV irradiation and the oscillatory nature of corona pulses in SF_6 are observed. Efforts are made to explain the results on the basis of the available knowledge of the mechanism of prebreakdown and breakdown phenomena. The rise time, fall time, and pulse magnitude depend upon pressure, distance, field nonuniformity and applied voltage. The smallest rise time of the order of 0.8 ns is observed in the case of corona pulses in SF_6 .

The pulse shape study is made in the presence of solid dielectrics (PTFE, PMMA and epoxy resin). The PD pulses observed are similar to those of breakdown pulses in longer gaseous gaps between electrodes. At lower gaps, the pulses are oscillatory and inconsistent in shape and magnitude. The

study of these pulses is useful in understanding the prebreakdown phenomena for the detection of faults in GIE with the help of broad-band detection system.

2.3. Corona under uniform field conditions

The effect of the material and the polishing grade of the electrode, pressure and type of the gas and the distance between electrode is studied in air, N_2 , O_2 , CO_2 , SF_6 , SF_6N_2 mixtures. It is observed that the prebreakdown pulses occur only in the presence of UV irradiation and an appropriate value of the current-limiting resistance. From the type of prebreakdown pulses present, it is possible to understand the nature of the electrode. Hence, the method is suggested to confirm the perfect cleanliness of the electrodes after mounting them in the test cell.

3. Conclusions

Breakdown voltage data in gases has been correlated in a relationship. An experimental set-up is designed for the detection of both prebreakdown and breakdown current pulses using broad-band detection having a time constant of 0.1 ns. Pulses with rise time of the order of 0.8 ns have been detected in SF_6 .

References

1. BOGGS, S. A. AND STONE, G. C. *IEEE Trans.*, 1982, E117, 120-128.
2. NEMA, R. S. *et al* *IEEE Trans.*, 1982, E117, 70-76, 434-439.

Thesis Abstract (Ph.D.)

Developmental studies on ZnO-based composites for surge-arrester applications by T. Asokan. Research supervisors: G. N. K. Iyengar (Deptt of Metallurgy) and G. R. Nagabhushana (Deptt of High Voltage Engineering).
Department: Metallurgy.

1. Introduction

Sintered ZnO-based ceramic composites containing several additive oxides like Bi_2O_3 , Sb_2O_3 , MnO_2 , Cr_2O_3 to name only a few, are known to exhibit high non-Ohmic behaviour and excellent surge withstanding capability¹. In view of these, ZnO-based composites have found extensive applications over the past decade, as nonlinear resistor elements in gapless surge arresters. Considerable literature is available to date on the physical and electrical properties of several ZnO-based composites^{2,3}. Despite this, the role of additive oxides on bulk density, microstructure and electrical properties is yet to be clearly understood. Further, influence of processing variables such as calcination, initial particle size and post-sintering on the overall performance of ZnO-based nonlinear resistor (NLR) is not well documented in the literature. Motivated by these considerations, the present work was undertaken to establish:

- (a) The influence of one or more additive oxides (Nb_2O_5 , Bi_2O_3 , Sb_2O_3 , CoO , MnO_2 , Cr_2O_3 , NiO , Al_2O_3 , BaO and SrO) on the microstructure, bulk density and electrical characteristics of ZnO. This part of the investigation has led to the development of the following ZnO-based composite, 0.1% Nb_2O_5 + 6% Bi_2O_3 + 3.5% Sb_2O_3 + 0.55% CoO + 0.7% MnO_2 + 0.9% Cr_2O_3 + 0.9%

NiO + 0.025% Al(NO₃)₃ + (balance) ZnO, designated as SM-Nb-ZnO NLR (selected multi-component ZnO-based system with Nb₂O₅) which was found to have good electrical properties characterised by high nonlinearity index, α , (≈ 40) and reasonable energy handling capability ($\approx 150 \text{ J/cm}^3$).

- (b) The effect of processing parameters such as calcination, initial particle size, sintering and post-sintering heat treatment on the overall electrical and physical properties of the system (SM-Nb-ZnO NLR) mentioned above.

2. Experimental procedure

The above objectives have been accomplished using the following experimental techniques:

1. The raw materials used in the present study were about 99.9% pure. The mixtures of oxides of desired composition were compacted at 300 kg/cm² and were sintered in air, in the temperature range from 900 to 1300°C. Calcination prior to sintering and post-sintering heat treatment was given to several multicomponent systems. The initial average particle size (1 to 5 μm) of the charge was controlled by varying the ball milling time (10 to 30 h). The electrical contacts were made on the samples using conductive silver paint.
2. Scanning electron microscopy (SEM), X-ray diffraction (XRD), electron spectroscopic chemical analysis (ESCA) and electron probe micro-analysis (EPMA) were employed to characterise the samples.
3. Current-voltage measurements (dc and pulse techniques) were made to study the nonlinear behaviour. Transmission line discharge method was used for assessing the energy handling capability. The life time was estimated by leakage current measurements. Values for the potential barrier height were obtained for ZnO-Nb₂O₅ binary and SM-Nb-ZnO + Li₂O multicomponent systems by resistivity measurements.

3. Composition development

Amongst the various ZnO-M_xO_y (where M is Nb, Bi, Sb, Mn, Co, Cr, Ba or Sr) binary systems investigated, ZnO-Nb₂O₅, ZnO-Bi₂O₃, ZnO-BaO and ZnO-SrO systems were found to exhibit nonlinear behaviour. The nonlinear behaviour in ZnO-Nb₂O₅ system is attributed to the formation of Zn₃Nb₂O₈ spinel phase. On the other hand, the origin of nonlinear behaviour in ZnO binary systems containing Bi₂O₃, BaO or SrO is found to be due to the formation of intergranular layer. Although the addition of Sb₂O₃, CoO or Cr₂O₃ to ZnO does not impart any nonlinear behaviour, it influences the microstructure, even in the presence of other additive oxides. Based on the results obtained for the binary systems mentioned above, the study was extended to the following ternary and multicomponent systems, with a view to understand the interplay of the additive oxides on electrical and microstructural characteristics of ZnO-based composites: ZnO + Nb₂O₅ + Sb₂O₃; ZnO + Nb₂O₅ + Sb₂O₃ + Bi₂O₃; ZnO + Nb₂O₅ + Sb₂O₃ + Bi₂O₃ + CoO; ZnO + Nb₂O₅ + Sb₂O₃ + Bi₂O₃ + CoO + MnO₂; ZnO + Nb₂O₅ + Sb₂O₃ + Bi₂O₃ + CoO + MnO₂ + Cr₂O₃ + NiO + Al₂O₃ (as Al(NO₃)₃). After a critical analysis of the results obtained for the above systems and using the information available in the literature, ZnO-based composite having the following composition was selected for further investigation: 0.1% Nb₂O₅ + 3.5% Sb₂O₃ + 6% Bi₂O₃ + 0.55% CoO + 0.7% MnO₂ + 0.9% Cr₂O₃ + 0.9% NiO + 0.025% Al(NO₃)₃ + (balance) ZnO (SM-Nb-ZnO). The sample having the above composition sintered at 1300°C was found to possess good nonlinearity ($\alpha \approx 40$) and a reasonable energy handling capability ($\approx 150 \text{ J/cm}^3$) compared to the rest of the systems studied in the present work. The phases identified in the above system include: (a) ZnO matrix, (b) Bi₂O₃-rich pyrochlore, (c) Zn₇Sb₂O₁₂ spinel, and (d) Zn₃Nb₂O₈ spinel. It was also observed that a part of bismuth

on the surface of the sintered sample was in the low oxidation state. From the above detailed studies, the effect of additive oxides can be qualitatively summarised as below:

Additive oxide	Effect	Comments
Nb_2O_5	$\text{Zn}_3\text{Nb}_2\text{O}_8$ spinel formation	Enhances the grain growth Improves nonlinearity
Sb_2O_3	$\text{Zn}_7\text{Sb}_2\text{O}_{12}$ spinel formation	Inhibits the grain growth
Bi_2O_3	Segregates at the grain boundary	Enhances the grain growth Improves the nonlinearity
CoO	Dissolves in all phases, prevents the evaporation of Bi_2O_3 , surface states	Improves the nonlinearity
MnO_2	Surface states	Improves the nonlinearity
Cr_2O_3 & NiO	Dissolve in $\text{Zn}_7\text{Sb}_2\text{O}_{12}$ spinel phase, stabilise the spinel phase	Control the grain size Increase the breakdown voltage
$\text{Al}(\text{NO}_3)_3$	Dissolves in ZnO matrix	Decreases the pore volume and ZnO resistivity Improves the energy handling capability

4. Role of processing parameters

The effect of the following processing parameters has been studied to improve NLR characteristics of SM-Nb-ZnO system: (a) calcination, (b) post-sintering and (c) initial particle size.

ZnO with 0.1 wt.% of Nb_2O_5 was calcined in the temperature range 1000 to 1200°C in air. The calcined charge was ball-milled and mixed with other additive oxides in the correct proportion, corresponding to the composition of SM-Nb-ZnO. The samples were prepared from this mixture in the usual manner. The samples prepared by calcination treatment at 1200°C were found to possess better electrical properties, compared to the rest including those prepared without calcination step. Therefore samples of this kind were selected to study the effect of post-sintering heat treatment.

Two types of post-sintering heat treatments were given to the samples: (a) cyclic post-sintering at 800°C for 6 h (3 times), (b) single step post-sintering at 1100°C for 10 h. The latter type of post-sintering heat treatment resulted in greatly reduced leakage current and significant improvement in stability which is attributed to the transformation of Bi_2O_3 from α to γ phase based on X-ray diffraction study.

The effect of initial particle size on the electrical properties of SM-Nb-ZnO NLR was studied as follows. As in the earlier case, $\text{ZnO} + 0.1\%$ Nb_2O_5 mixture was calcined at 1200°C followed by ball-milling and sieve analysis. The material (-400 mesh) was mixed with other additive oxides and further ball-milled for different durations (10 to 30 h) to reduce the particle size. The samples were prepared from the above ball-milled mixture in the usual way. The samples after sintering were subjected to post-sintering heat treatment at 1100°C for 10 h. The samples prepared from the 30 h ball-milled mixture were found to possess better electrical and physical characteristics compared to the rest. At this stage of development, the following characteristics were accomplished: leakage current ≈ 3 to $4 \mu\text{A}$, nonlinearity index (α) ≈ 60 , voltage ratio ≈ 1.88 , energy-handling capability $\approx 300 \text{ J/cm}^3$.

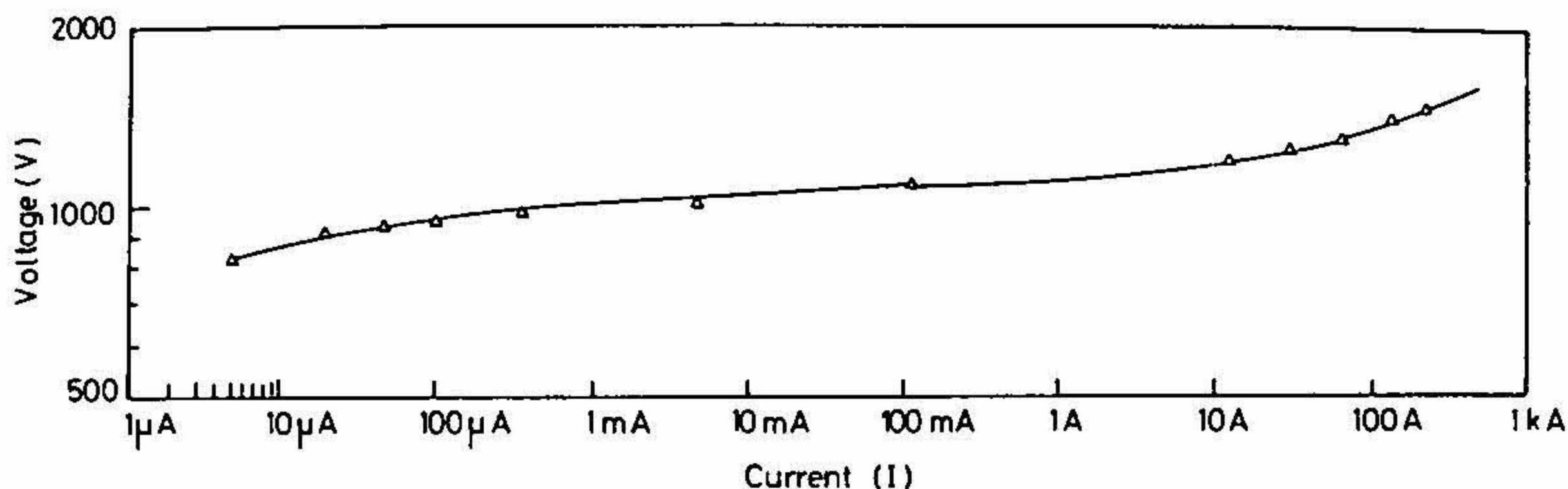


FIG. 1. V-I Characteristic of the sample containing 0.2 wt% Nb_2O_5 (ball milling time - 30 h).

It was felt that there was still scope for improving the degradation characteristics without sacrificing the other properties by a judicious choice of Nb_2O_5 content, keeping all other parameters including the proportion of other additive oxides constant. The Nb_2O_5 content was varied from 0.1 to 0.3 wt.% and the ball-milling time was also varied from 10 to 30 h. It was found that the sample containing 0.2 wt.% Nb_2O_5 and ball-milled for 30 h was found to possess the best overall characteristics, as summarised below: leakage current 1 to $2\ \mu\text{A}$, nonlinearity index (α) ≈ 60 , voltage ratio ≈ 1.67 , energy-handling capability $\approx 325\ \text{J}/\text{cm}^3$ and life time ≈ 150 years at 50°C . The V-I characteristic of this sample is shown in fig. 1. An insignificant increase in leakage current, to a final value of 2 to $3\ \mu\text{A}$, was observed after subjecting the sample to high-energy pulses of $325\ \text{J}/\text{cm}^3$. These characteristics are considered to be very satisfactory from the point of field usage. Some of the characteristics such as leakage current and energy-handling capability achieved in the present work are believed to be superior to those of the commercial ZnO-based NLR elements currently in use.

References

1. MATSUOKA, M. Nonohmic properties of ZnO ceramics, *Jap. J. Appl. Phys.*, 1971, 10, 736-746.
2. LEVINSON, L. M. AND PHILIPP, H. R. The physics of metal oxide varistors, *J. Appl. Phys.*, 1975, 46, 1332-1341.
3. EDA, K. Conduction mechanism of non-ohmic ZnO ceramics, *J. Appl. Phys.*, 1978, 49, 2964-2972.

Thesis Abstract (Ph.D.)

Elastic analysis of contact between nominally flat rough surfaces using finite element method
by T. Krishnamurthy.

Research supervisor: M. R. Raghavan.

Department: Mechanical Engineering.

The surface texture has a profound influence on friction and lubrication of surfaces in relative motion, contact resistance (thermal and electrical), wear and fatigue strength. When freshly machined surfaces are brought into contact and loaded, the contact may be fully plastic or elastoplastic or fully elastic

depending upon the surface roughness. For smooth fresh surfaces the loaded contact may be expected to be entirely elastic. In rough surfaces, even though the contact in the first cycle is plastic, as the plastic flow is irreversible, the contact has to be entirely elastic after a few cycles of loading. Thus the study of elastic behaviour of rough surfaces under loaded contact is of great practical significance.

The elastic contact between nominally flat rough surfaces has been analysed by several investigators. In all these investigations the asperities are assumed to have simple geometrical shapes like spheres, paraboloids and elliptic paraboloids and the asperity peak heights conform to some statistical distribution function. In all these studies, the elastic behaviour of asperities having the above-mentioned shapes is assumed to be according to Hertzian theory. Tallian has studied the elastic behaviour of contact between an infinite wedge with cylindrical tip and a rigid plane. However, no study of the elastic behaviour under loaded contact of wedge-shaped asperities (with cylindrical tip) or conical asperities (with spherical tip) of finite height and supported by bulk of finite or infinite depth has been reported in the literature. The author has evolved an analytical procedure using the finite element method for solving problems involving elastic contact between bodies with identical geometry. He has studied using this procedure, the elastic contact between a rigid plane and a wedge-shaped asperity of finite height protruding from infinite bulk and evolved equations for defining the deformation and stresses for both contact in the curved tip and flank regions of the asperity. Also he has made a study of the elastic contact between a rigid plane and a conical asperity protruding from an infinite bulk and equations for defining the deformation stresses for both contact in the curved-tip and flank regions have been evolved. The geometry of the wedge- and conical-shaped asperities is completely defined by the parameters, curved depth factor λ or tip radius R , flank angle θ and the asperity height h . Here λ defines the fraction of the height of the asperity occupied by the curved tip. It is found that the curved depth factor λ correlates the deformation characteristics of both wedge- and conical-shaped asperities better than the parameters, R and θ . The curved depth factor λ clearly defines the compliance Δ up to which the contact is within the curved-tip region of the asperity. When contact is in the curved-tip region, while the deformation in a conical asperity is governed only by the tip radius, it depends on both λ and tip radius in a wedge-shaped asperity. However, the stresses in both wedge-shaped and conical asperities are dependent only on the tip radius. On the basis of these analyses two deformation models are proposed to predict the onset of plastic flow in a real surface at elastic levelling. In the first model the onset of plastic flow can occur either in the asperity or in the bulk, while in the second model, the onset of plastic flow is constrained to occur within the bulk material. The maximum flank angle of the asperities in the real surface up to which the deformation of the surface is elastic right up to the levelling of all asperities in the surface predicted on the basis of these models, is considerably higher than the corresponding Halliday angle.

The contact between two nominally flat rough surfaces is analysed on the basis of contact between a rigid plane and a model rough surface having asperities with Gaussian peak-height distribution and constant tip radius. The contact is restricted within the curved-tip region of the asperities and the asperity interaction effects are ignored. This study revealed the following:

- i) The relation between the real area of contact and load is approximately linear. The real pressure remains approximately constant when the contact plane is located above the mean plane of the rough surface. However, there is a sharp increase in the real pressure when contact extends below the mean plane of the rough surface.
- ii) Using the procedure evolved by Greenwood and Williamson for defining the plasticity index ψ at which the elastic-plastic transition occurs in a real surface, the author could develop an expression for ψ for real surfaces with conical asperities and with wedge-shaped asperities.
- iii) It is found that the limiting minimum value for the parameter $(E^*/H)(\sigma/R)^{1/2}$ (where σ is the standard deviation of the peak-height distribution, E^* the effective modulus and H the

hardness of the surface material) at which a surface with wedge-shaped asperities deform plastically at very light loads is about 3.7 times higher than the corresponding value for a surface with conical asperities. Also the limiting maximum value for $(E^*/H)(\sigma/R)^{1/2}$ for a surface with wedge-shaped asperities to deform elastically at higher loads is about 3.0 times greater than the value for a surface with conical asperities. At any load, it is observed that the real area of contact in the surface with wedge-shaped asperities is 2.2 to 2.9 times greater than that in a surface with conical asperities having the same value of parameter $(E^*/H)(\sigma/R)^{1/2}$.

- iv) Two deformation models are used for defining at any separation m_c or plasticity index ψ , the limiting or maximum flank angle to the asperities in a real surface, up to which the deformation of the surface is elastic. In the first model, the onset of plastic flow can occur at any point in the asperity or bulk material. In the second model the onset of plastic flow is constrained to occur at the interface between the critical asperity and the bulk. Expressions for the limiting flank angle corresponding to these deformation models have been developed and data on the limiting flank angle for various material-surface parameters have been provided. At any plasticity index ψ , the maximum flank angle up to which the surface behaves elastically, decreases as E^*/H increases.
- v) The location of the point at which the onset of plastic flow occurs in a surface is a function of λ , ψ and E^*/H . In surfaces with wedge-shaped asperities prepared from material with $(E^*/H) > 100$ and $\psi < 1.5$ the onset of plastic flow always occurs within the bulk material; the corresponding minimum E^*/H value for surface with conical asperities is 16. In such materials *e.g.* aluminium ($E^*/H = 365.0$) and mild steel ($E^*/H = 111.0$), the bulk material undergoes considerable plastic deformation before the plastic zone spreads to the asperity.

Thesis Abstract (Ph.D.)

Improved performance current source inverter-fed induction motor drives for industrial applications by S. K. Biswas.

Research supervisors: B. S. Ramakrishna Iyengar and N. J. Rao.

Department: Electrical Engineering.

The present trend towards increased application of variable speed inverter-fed induction motor drives in industry has prompted research towards further refinement of their operating characteristics. It has been known for a long time that the speed of an induction motor (the most popular machine for industrial applications) can be varied by changing its supply frequency. However, to maintain constant torque capability throughout the varied speed range, the supply voltage has also to be varied in coordination with the frequency. Several schemes involving rotary-frequency changers were developed, but they did not become popular with the industry due to maintenance problems. With the development of thyristors, compact and reliable static-inverter circuits were introduced, which utilised closed-loop control schemes for superior performance of the drives. The work presented in this thesis is related to the development and analysis of improved performance current-source inverter-fed induction motor drives for industrial applications. Two approaches, namely, development of new control strategies and development of new converter structures, have been followed.

The work reported in this thesis starts with a review of some of the existing CSI drive systems used in industry, the design of which is based on the conventional steady-state analysis using phasors. These are well suited to applications not demanding high dynamic performance. In particular, schemes without tachogenerator feedback are industrially preferred, due to the lack of space for mounting a tacho and its maintenance problems. Compared to the voltage-source inverter-fed induction motor,

the CSI drive cannot be operated in open-loop and hence the closed-loop circuitry is preferred to be as simple as possible in order to compete with open-loop VSI-fed drives. Many tachless control schemes have been designed in the past, but they usually have poor speed regulation and transient response. A new tachless simple control scheme is proposed, using a method of slip compensation for speed regulation and a torque feedback for better transient response. The torque is calculated from the dc link power and the inverter frequency signal, while the slip compensation is proportional to the torque under constant flux operation.

An analysis of the current-fed induction motor is made using the method of space (or park) vector, both for the steady-state and transient conditions. From this analysis, the principle of vector-decoupled control is established. It is shown that the dynamic behaviour of the induction motor becomes similar to that of a separately excited dc machine by exercising control such that the stator-current vector is fixed in position with respect to the rotor-flux vector. New control techniques for CSI drives based on the above analysis have been described with their theoretical basis and hardware implementation. The conventional auto sequentially commutated inverter (ASCI) has been used for this purpose, while the closed-loop control strategies are oriented towards three different objectives:

1. High dynamic performance (using the principle of field orientation),
2. High efficiency operation (using a torque feedback with current reference derived through a function generator circuit), and
3. Constant slip frequency control (using a method of adjusting the stator power factor angle) with scope for eliminating a tacho feedback.

A microcomputer has also been used to simplify the control hardware.

The principle of field orientation has been explained, as applied to a CSI-fed induction motor. The various options for orientation of the stator-current vector are analysed and it is shown that orientation with the rotor-flux vector alone gives total decoupling of the flux and torque-producing components of the stator-current. The methods of implementing this orientation are discussed and a control scheme is presented for the field-oriented control of a CSI-fed drive. The scheme has been experimentally verified and the results are presented.

In drive systems not requiring high-dynamic response, a high-operating efficiency is desirable. In this connection, the space vector analysis of the motor operation with a CSI supply is used to highlight the control principle to be adopted for obtaining the maximum efficiency over the full operating range. The implementation details of the new control principle are also presented.

Using the space vector analysis of the current-fed induction motor, it is shown that if the torque angle is maintained constant in the motor, then the control scheme can be substantially simplified, since the machine will run at a constant slip frequency. This concept is used to design new control schemes for the CSI-fed induction motor drive, where the tachogenerator speed feedback can be disposed and a fixed slip compensation signal used for maintaining speed accuracy. The constant angle control is implemented by exercising control over the stator power factor angle of the motor, when fed from the CSI system.

The torque ripple in an ASCI-fed drive, caused by the harmonics of the motor-line current, causes operational problems at low speeds. New current pulse width modulation (PWM) techniques have been proposed for reducing the torque ripples and simultaneously achieving a fast sub-cycle current control in the inverter circuit. This allows the current control loop to be implemented through the inverter itself without depending on the slow response dc link adjustments. However, to facilitate implementation of a wide range of current PWM patterns, a new form of CSI circuit has been proposed and its operation verified through testing of a prototype. The new circuit uses three

one-phase CSI bridges connected in series to the same dc link but with each phase feeding the isolated windings of a standard three-phase induction motor. This arrangement ensures identical current magnitude in each phase while removing the interdependence of the PWM pattern implementation between the phases.

The thesis is concluded by suggesting work for further investigations which may lead to the realisation of better drive systems for the industry.

Thesis Abstract (M.Sc.(Engng))

Holographic interferometric study of natural convective heat transfer in vertical rectangular enclosures by N. G. Patil.

Research supervisors: C. R. Prasad and V. H. Arakeri.

Department: Mechanical Engineering.

1. Introduction

In many applications such as thermal insulation of buildings, double-glazed windows and in flat-plate solar collectors, natural convective flows, induced by buoyancy forces on the fluid, are encountered. An analysis of the problem reveals that the flow and heat transfer here are defined by three dimensionless parameters: Rayleigh Number Ra_L , Prandtl Number Pr and the enclosure height-to-width aspect ratio H/L . Optical techniques like interferometry, shadowgraphy and schlieren are commonly used in investigations¹ of fluid flow and heat transfer. The change in refractive index of the fluid caused by temperature and density changes is the basis of these methods. Such non-intrusive probes have several advantages over mechanical probes, like high-spatial and temporal resolution, absence of probe-induced perturbations, etc. Although Mach-Zehnder interferometers are frequently employed for heat transfer studies the need to maintain nearly identical path length in the two limbs (thus requiring two identical cells with optically flat windows, one cell being used for compensation) has limited its application mainly to studies in air. Holographic interferometry, on the other hand, is especially well suited to studies with transparent fluids since there is no need for special windows or cells. In the present work, heat transfer in water-filled vertical rectangular enclosures of moderate aspect ratios has been studied using holographic interferometry.

A large body of work on natural convection in rectangular enclosure is available in literature. The first major theoretical analysis was that of Batchelor². He showed that the flow within the cavity can be grouped into three different (conduction, transition or asymptotic and boundary layer) regimes in the laminar region, depending upon the values of Ra_L and H/L . For small values of $Ra_L/(H/L)$, (Rayleigh Number $Ra_L = g \beta L^3 \Delta T / \nu a$, where g is acceleration due to gravity, β the expansion coefficient, $\Delta T = T_h - T_c$ the difference in temperature of the two walls, a the thermal diffusivity and ν the kinematic viscosity of the fluid) the conduction regime is observed, wherein the temperature change is linear between the two walls except near the top and bottom ends where convective flow occurs. As $Ra_L/(H/L)$ is increased, the temperature profiles become curved throughout, indicating that convection is occurring over most of the enclosure height. Here the two thermal boundary layers on the vertical walls merge at a short distance from the two ends giving rise to the asymptotic regime². With further increase in $Ra_L/(H/L)$ the boundary layer regime occurs wherein the flow is confined close to the walls with an interior region of stratified core, having a uniform positive vertical temperature gradient along the central line of the cavity. Recent work³ has shown that conduction regime is observed for $Ra_L/(H/L)$ below 500, while the boundary-layer regime is seen for $Ra_L/(H/L)$

above 3,300, with the asymptotic flow in between³. An increase of this parameter ($> 25,000$) finds the establishment of small secondary flow cells at the side walls and above 75,000 secondary cells³ are seen even in the centre. The changes in the flow regimes noted above strongly influence the local heat-transfer coefficient h . Although numerous experiments on natural convection in rectangular enclosure have been performed, there still exists a lack of agreement between the heat-transfer correlations. Furthermore, not much information on variation of local heat-transfer coefficient along the heated surface is available. Here a systematic study of heat transfer for a wide range of Rayleigh Numbers and aspect ratios has been carried out experimentally to clarify these points.

2. Holographic interferometry

A holographic interferometer was developed for visualizing the temperature fields in rectangular fluid-filled differentially heated enclosures. Figure 1a is the schematic of the set-up used for our work. A hologram is recorded by adding to a coherent object wavefront U_o , a coherent reference wavefront U_r , and photographing the resulting intensity pattern in a plane (x, y) . A replica of $U_o(x, y)$ is reconstructed on illuminating this hologram with only U_r . Two wavefronts, U_o and U'_o , one corresponding to the wavefront passing through the unheated fluid and the other through the heated fluid, are recorded sequentially in time on a single hologram. Such a double-exposed hologram yields an interferogram of the interference between U_o and U'_o , on reconstruction with U_r . A diffuser (ground glass plate) placed behind the test section allows observation of the hologram from many directions, thus furnishing interferometric data for rays traversing the test section in different directions. The rectangular cell used in our study (fig. 1b) consists of two copper plates kept apart with perspex spacers. The walls are kept isothermal at T_h and T_c , with the help of thermostatted water baths. Since the interference is between U_o and U'_o , the phase variations due to imperfections in windows do not affect the interference fringe pattern; hence ordinary plate glass windows are used. A 15 mW He-Ne laser (Spectra Physics 124 B) was the source. The object beam was spatially expanded and filtered before passing through a mylar diffusing screen. Holograms were recorded on Agfa 10E75

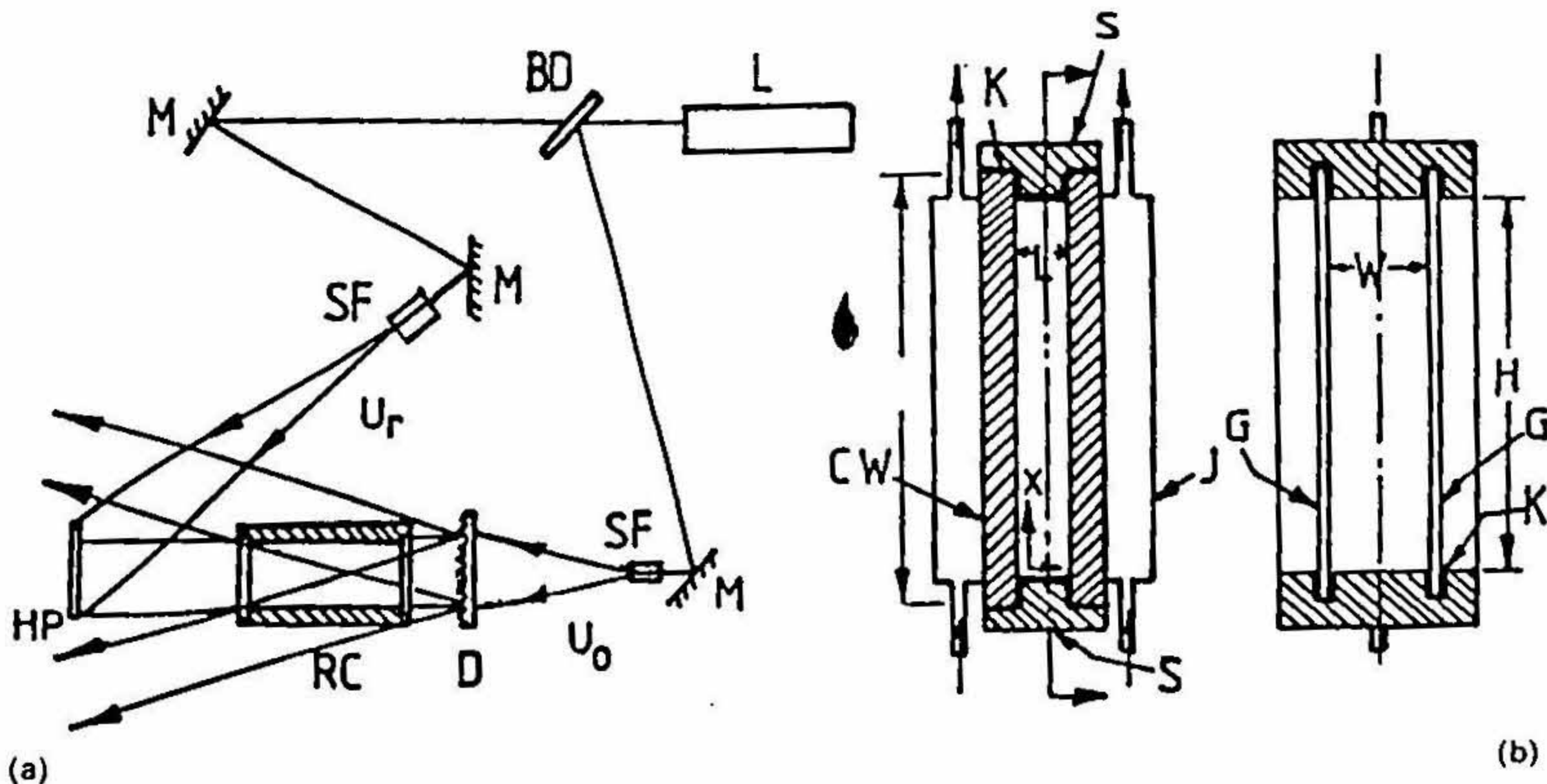


FIG. 1a. Schematic of holographic interferometer. L = Laser, BD = Beam divider, M = Mirror, SF = Spatial filter; D = Diffuser, RC = Rectangular cell, HP = Holographic plate. b. Details of cell RC. CW = Copper walls, J = Water jackets, S = Spacer, W = Glass windows.

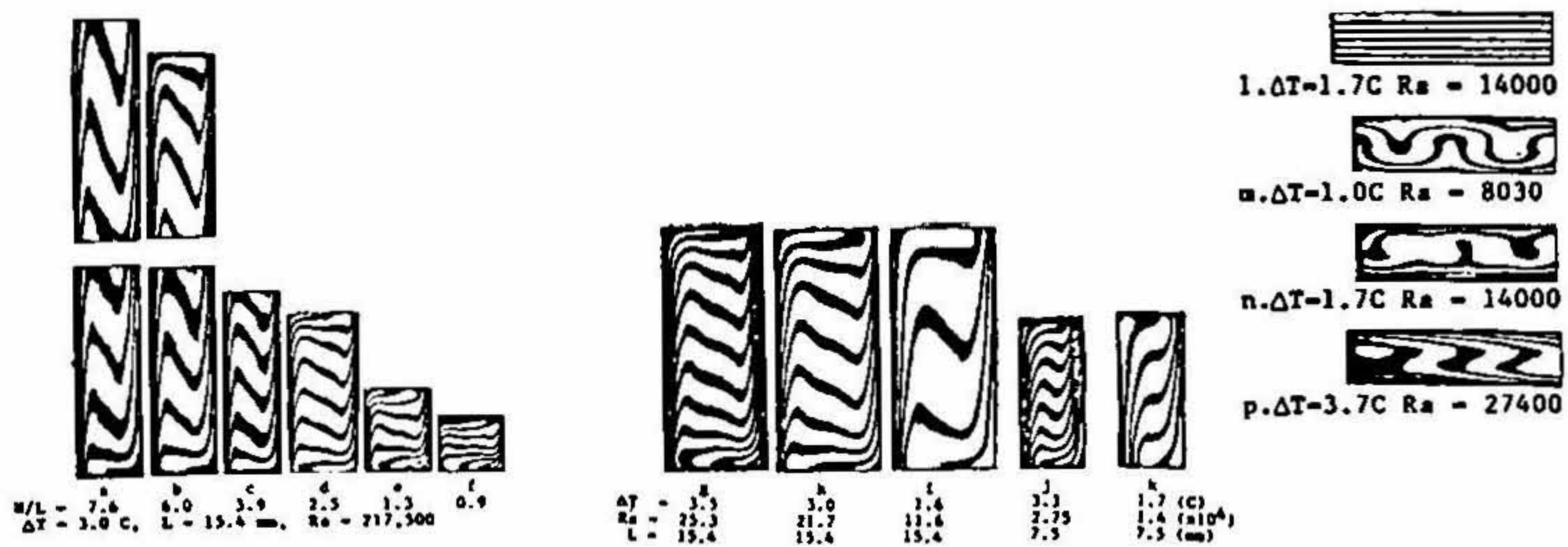


FIG. 2. Isotherms (interferograms) for rectangular enclosure, a to k: enclosure vertical, l to p: enclosure horizontal, l: top horizontal wall heated, m to p: bottom wall heated.

plates. The first exposure of the holographic plate is made with water inside the cell and both walls held at T_c . Then one wall is heated to T_h and a second exposure is made after attaining steady state. Reconstruction of the double-exposed hologram yields the interferograms shown in fig. 2. The fringes represent the contours of the isotherms. Temperatures are derived from the interferogram by using the relation between refractive index (n) and density of fluid (Lorentz-Lorenz equation¹). Since dn/dT is almost constant for the small range of temperatures the fringe number N is related to the temperature by

$$T - T_{ref} = (N\lambda/W)(dn/dT)^{-1}$$

where λ is the wavelength of laser (632.8 nm) and $dn/dT = 9.85 \times 10^{-5} \text{ C}^{-1}$ at 25°C . For the figures, 2a-p, the difference in temperature between two neighbouring isotherms is about 0.23°C .

3. Results and conclusions

Experiments were conducted for the following range of parameters: aspect ratio $H/L = 0.86 - 15.8$ and $W/L = 1.8 - 3.75$; $Ra_L = 1.25 \times 10^4 - 2.74 \times 10^5$; $T = 1.4 - 3.8^\circ\text{C}$; Prandtl Number (ratio of kinematic viscosity and thermal diffusivity) = 5.85. Figure 3a shows the temperature profiles (derived from the interferograms using the relation given above) for $H/L = 2.5$ while fig. 3b shows h in the dimensionless form Nu_L the local Nusselt Number ($Nu_L = hL/k$, and $h = (dt/dY)_{Y=0}$ the slope of the temperature profiles in fig. 3a at $Y = 0$). The bottom of the hot plate and top of the cold plate where maximum values of Nu_L occur are the starting corners while the other two are the departure corners. A comparison of the interferograms in figs. 2a, d and e with the numerically computed⁴ isotherms in fig. 4 show excellent qualitative agreement with the predicted values⁴. For $Ra/(H/L) 75000$ (figs. 2d to h) secondary flows are seen within (corresponding to the inflections in isotherms). Figure 2l is the interferogram for a horizontal fluid layer heated from above and shows pure conduction, while 2m, n and p are for the fluid heated from below (the well-known Rayleigh problem of thermal instability). Multicellular (Benard) flow is observed in 2m and n while in 2p unicellular flow is seen. Figure 5 illustrates the effect of aspect ratio on average Nusselt Number for a fixed Ra_L of 2.17×10^5 . Nu_L decreases with an increase in the aspect ratio because the bulk of the heat transfer to the fluid occurs near the bottom of the heated wall and an increase in the height of the enclosure does not significantly increase the total heat transfer. There is in excellent agreement with Newell and Schmidt's⁴ numerical results. Variation of Nu_L with Ra_L is shown in fig. 6. This conforms to the power law correlation like $Nu_L = \text{const} (Ra_L)^{0.25} (H/L)^{-0.25}$ which has been proposed by some authors.

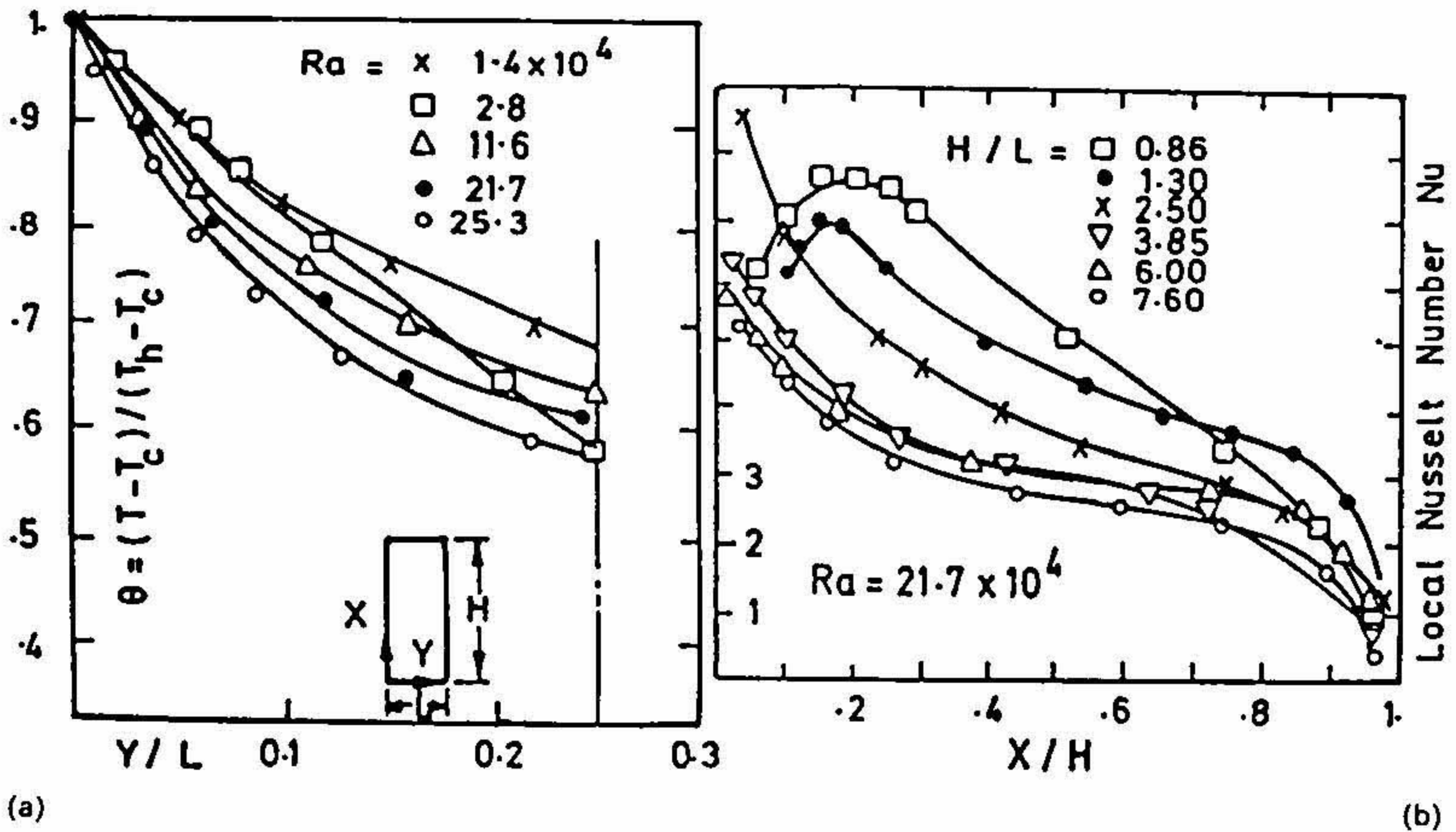


FIG. 3a. Temperature profiles across vertical enclosure for water. b. Variation of local heat transfer coefficient (Nu_x) along heated vertical wall.

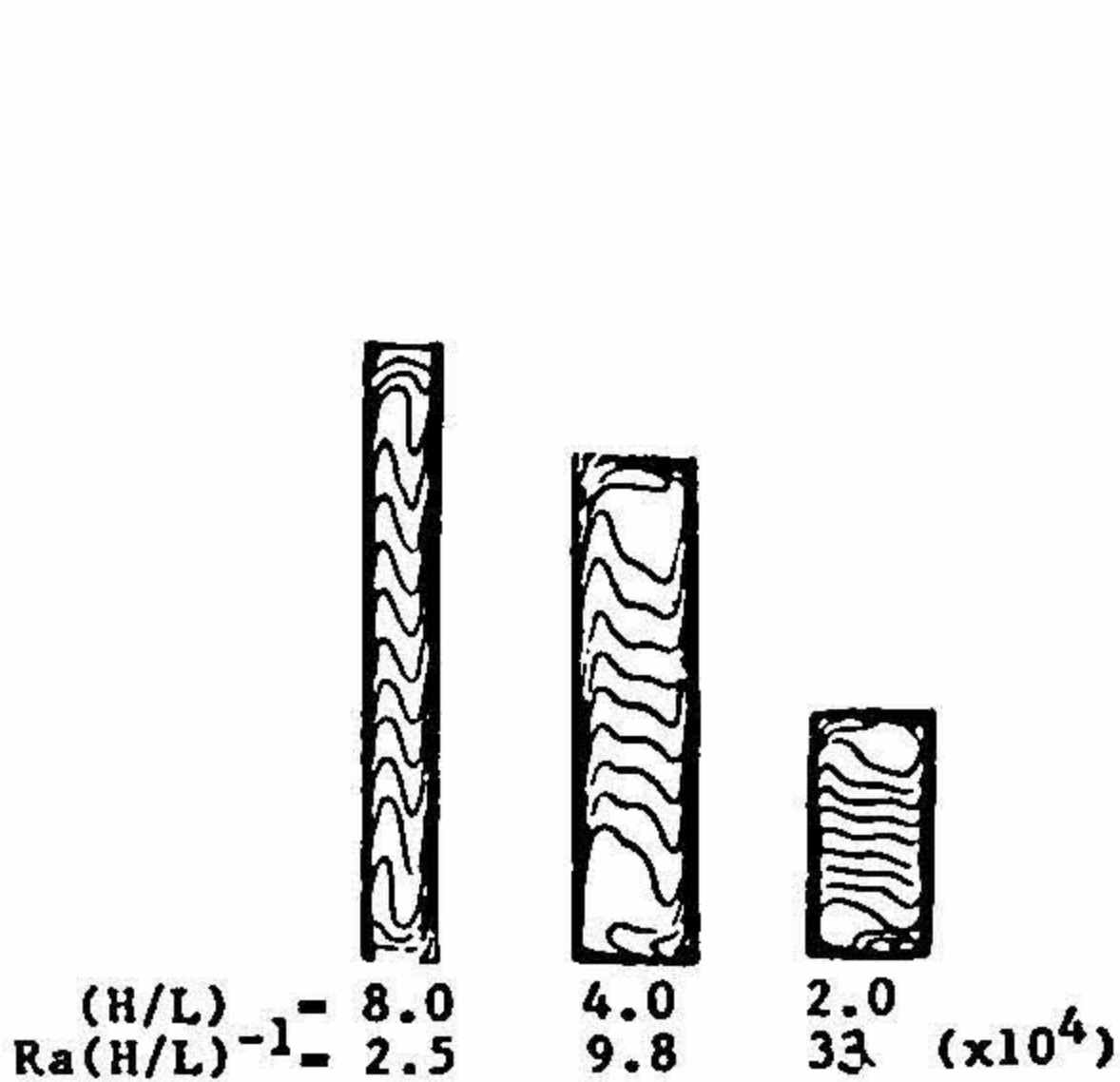


FIG. 4. Theoretically computed isotherms.

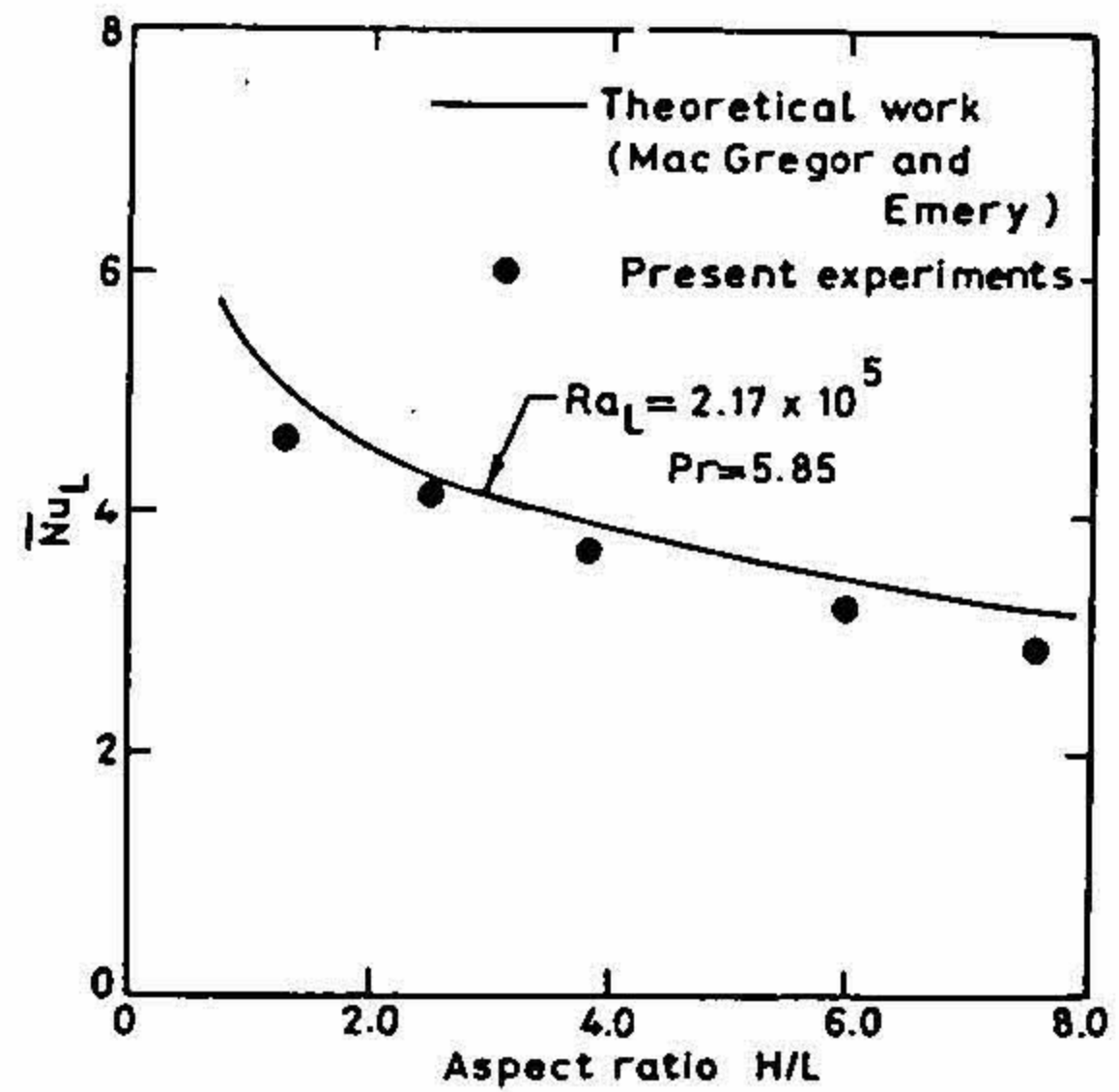


FIG. 5. Average Nusselt Number vs aspect ratio.

This study has shown the effectiveness and simplicity of holographic interferometry for visualization and quantifying heat flow in fluids in a two-dimensional situation (*i.e.*, fluid properties are invariant in the z direction). Using this technique the different regimes in natural convection have been clearly delineated and heat-transfer coefficients have been obtained. This work has also established the validity of some of the numerical studies and shown that some others are incorrect.

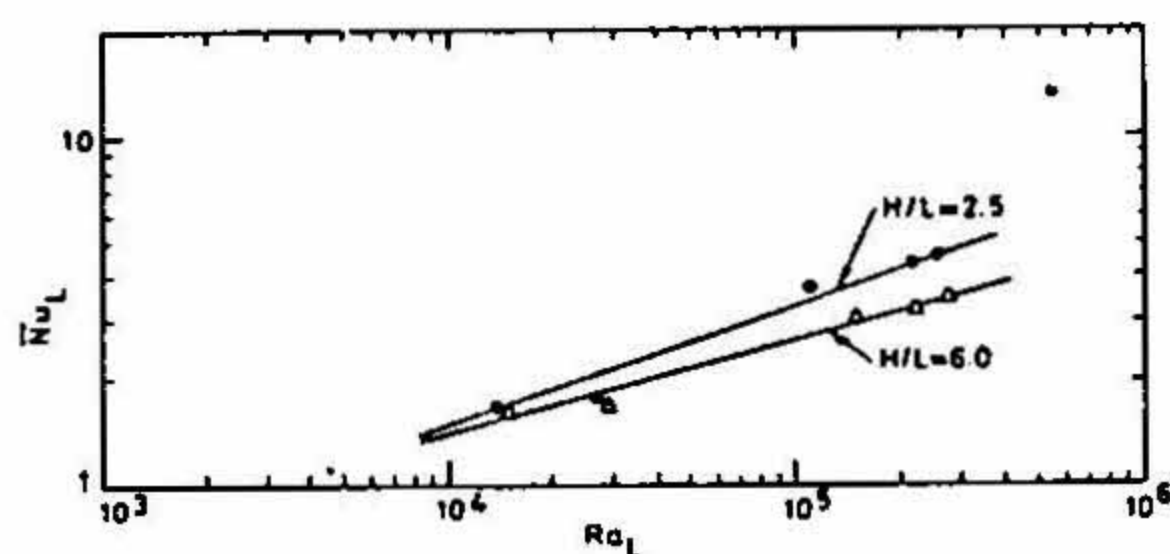


FIG. 6. Average Nusselt Number, Nu_L vs Ra_L .

References

1. ECKERT E. R. G. AND CARLSON, W. O. Natural convection in an air-layer enclosed between two vertical plates with different temperatures, *Int. J. Heat Mass Transfer*, 1961, 2, 106-120.
2. BATCHELOR, G. K. Heat transfer by free convection across a closed cavity between vertical boundaries at different temperatures, *Q. Appl. Math.*, 1954, 12, 209-233.
3. SCHINKEL, W. M. M., LINTHORST, S. J. M. AND HOOGENDOORN, C. J. The stratification in natural convection in vertical enclosures, *ASME J. Heat Transfer*, 1983, 105, 267-272.
4. NEWELL, M. E. AND SCHMIDT, F. W. Heat transfer by laminar natural convection within rectangular enclosures, *ASME J. Heat Transfer*, 1970, 92, 159-168.

Thesis Abstract (M.Sc.(Engng))

Coherent optical image deblurring with computer-generated Fourier plane filters by A. Senthil Kumar.

Research supervisor: A. Selvarajan.

Department: Electrical Communication Engineering.

1. Introduction

One of the most interesting aspects of modern communication is the transmission, storage and retrieval of the information in 'pictorial form'. A photographic image can be viewed as an information carrier coded as grey-level variations. In an ideal situation, one gets an image of high definition with a good-quality imaging optics and controlled photographic processing. In practice, sometimes the image is degraded due to the atmospheric turbulence, defocussing, camera motion, camera lens aberrations, etc. The result is a blurred picture that may appear, at first sight, to have lost the desired information. Both digital¹ and optical² techniques are reported in the literature to restore the information from such blurred pictures. This thesis is concerned with images that suffer from linear camera motion and defocussing blurs and optical techniques that compensate for these blurs using a coherent optical processing system (COPS).

2. Experiments and discussion

The following three steps are generally involved when the COPS is used to achieve a data processing task. (1) The given picture to be processed is kept at plane P_1 (fig. 1) and Fourier transformed with

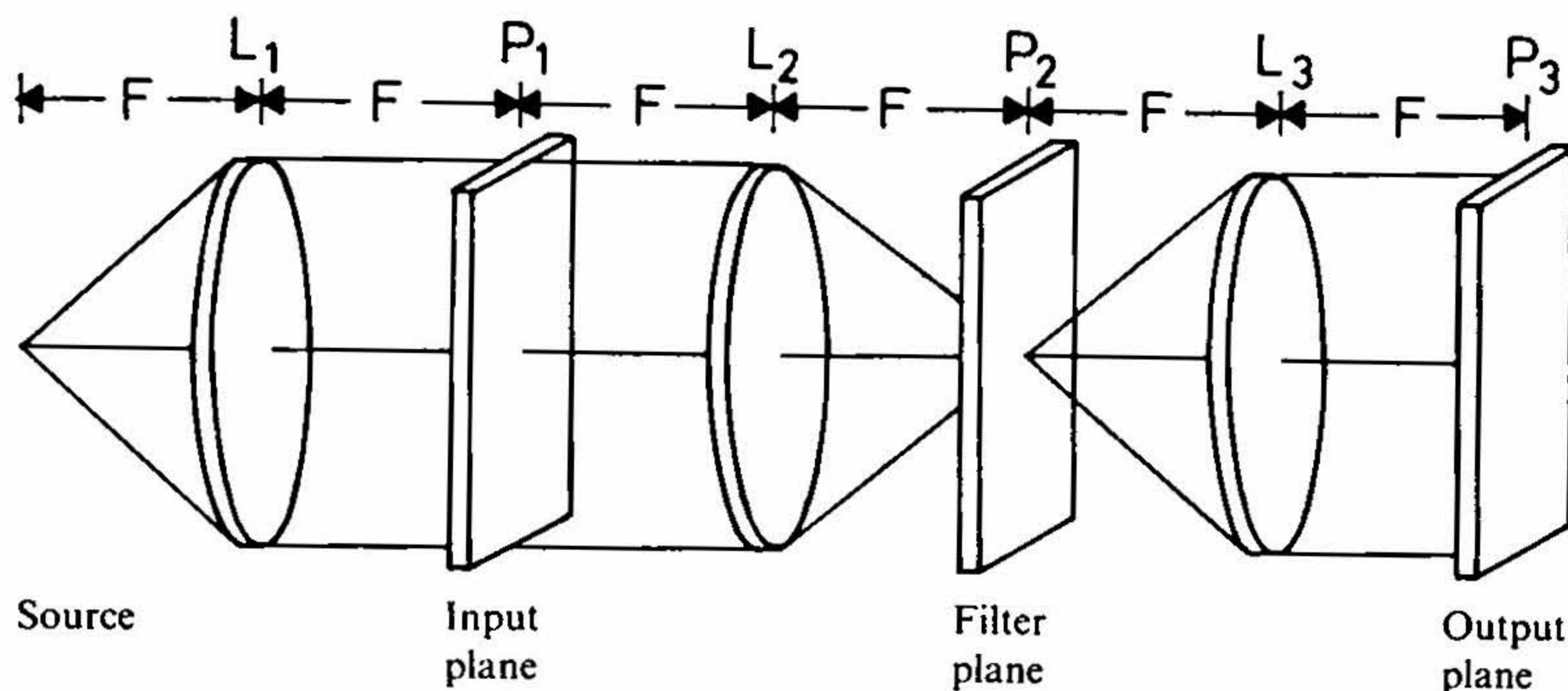


FIG. 1. A coherent optical system for image deblurring.

a lens L_1 , (2) a spatial filter of a known impulse response is introduced at plane P_2 , and (3) the light emerging out from the spatial filter is again Fourier transformed with the lens L_2 to obtain the processed image.

One of the methods of optical image restoration is through inverse filtering (or equivalently through Wiener filtering for noise suppression). In the present study, methods of fabricating inverse and Wiener filters are discussed. Because of the flexibility and accuracy, the special emphasis is on those that are aided by a digital computer.

Deblurring filters, for the general case, can have complex amplitude transmittance. For the two chosen blur types (linear motion and defocussing), however, they are simple, real functions but not nonnegative. Hence the phase part of the filter is represented by 0 and π depending on whether the function is positive and negative, respectively. Two ways of realizing the filters are: first, by fabricating both amplitude and phase parts of the filter separately and sandwiching them together, and second, by generating the filter directly as a hologram realised either optically or digitally.

Sandwich filters: The phase-only filters are obtained as modulated gratings using the principle of the 'de-tour phase'³. The filters are designed using a computer-aided plotter with special care taken on their space-bandwidth product to be greater than that of the object. For the blur width chosen (0.6 mm), it has been found to be satisfactory if the filter width covers three sidelobes of the blur function on either side of the spectral plane origin (fig. 2). The amplitude part of the filter is generated following the methods of Vasu⁴. Our experiments showed that the phase filter plays a vital role in deblurring; the Wiener filters, as expected, produced noise-free deblurred outputs whereas the inverse filters gave sharper outputs though corrupted by noise.

Digital holographic filters: In another development, the deblurring filters are fabricated as double-phase digital holograms⁵. This hologram has only two subcells in each resolution cell that represents a discrete value of the filter, and has the advantage of the least computation time when compared to the Lee's four subcell or Burckhardt three subcell holograms³. In addition, since the 1:1 black-to-white ratio of the double-phase hologram (DPH) is maintained in each cell and hence the hologram as a whole, the diffraction efficiency is higher than that of the Lohmann hologram.

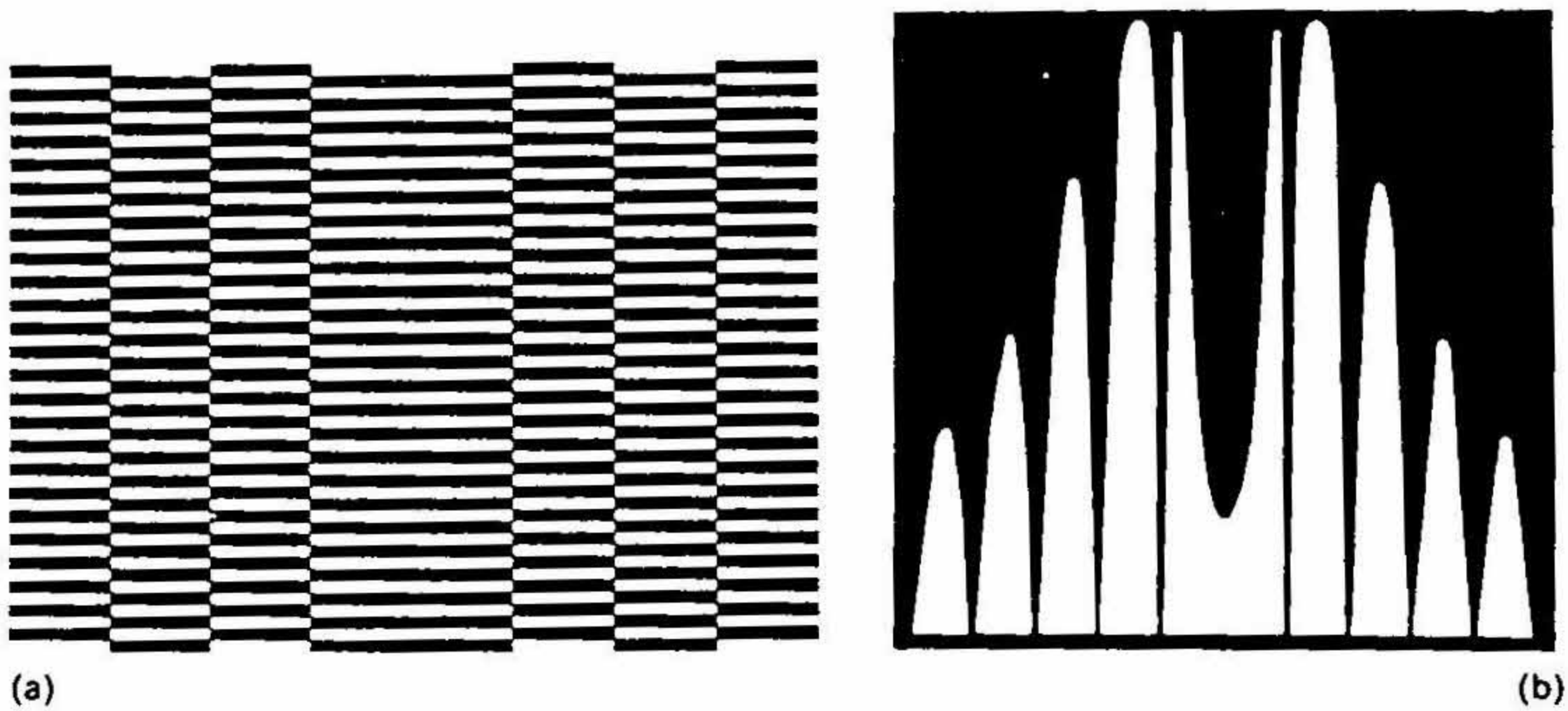


FIG. 2. (a) Phase-only filter and (b) binary pattern for generating amplitude Wiener filter for linear camera motion blur.

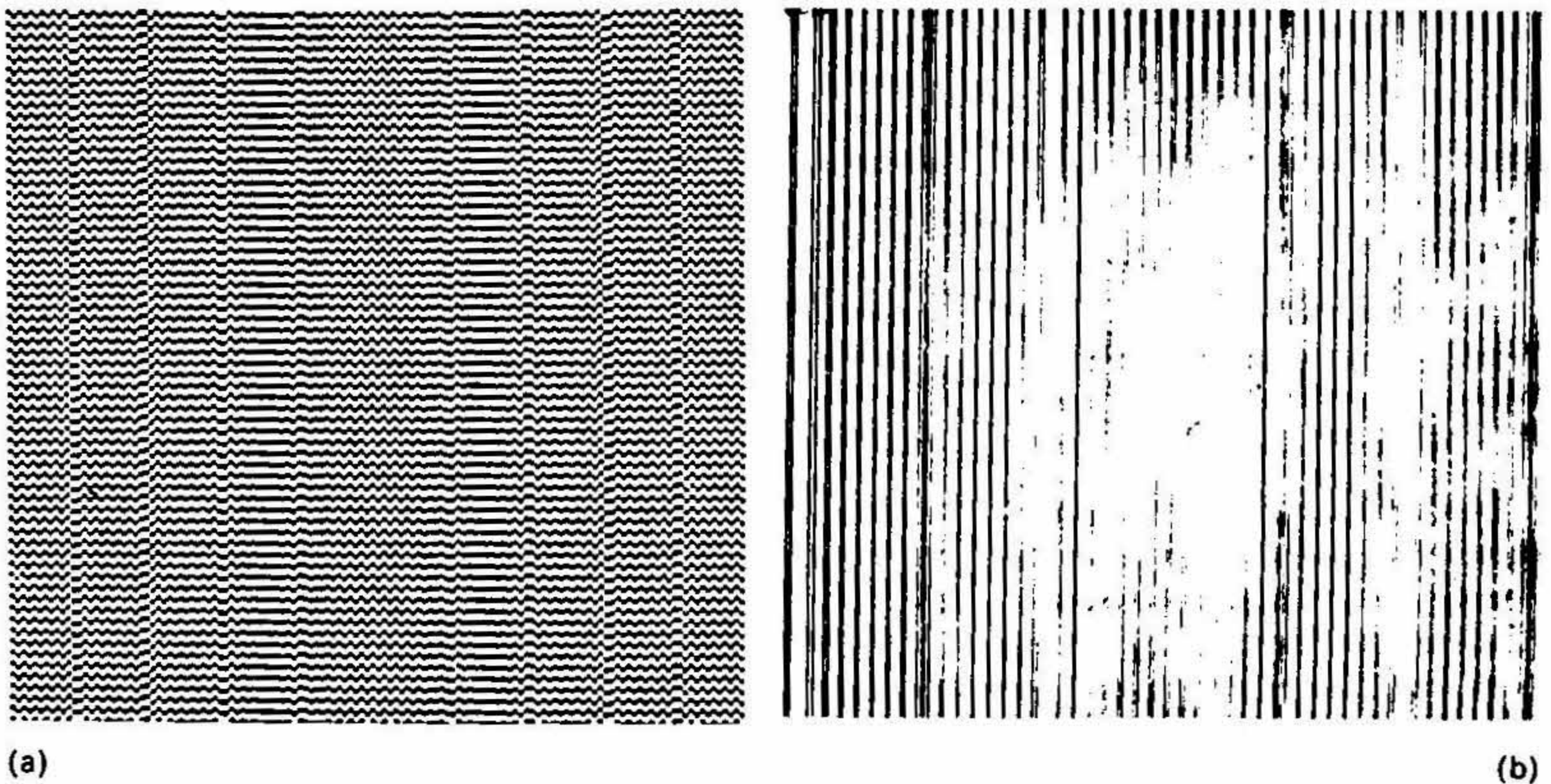


FIG. 3. The Wiener DPH filters for linear motion blur according to: (a) the present scheme, and (b) the Vasu-Rogers scheme.

Through an analysis of amplitude quantisation error in DPH, it is found that coding the square root of the filter amplitude helps to reduce the error only between the amplitude range from zero to $(1/3)$. A DPH for the whole amplitude is generated with circular overflow correction³. The DPH filter proposed for square-root coding⁶ is also developed for comparison. The Wiener filters generated for this study are given in fig. 3. The results shown in fig. 4 reveal that even though the DPH generated for full amplitude brought out sharpness in the output, the deblurring is not complete when compared to that of the Vasu-Rogers filter⁶. It can be concluded that there could be an error, due to the circular overflow correction, in the phase shift of the filter while switching from the positive to negative values or *vice versa*.

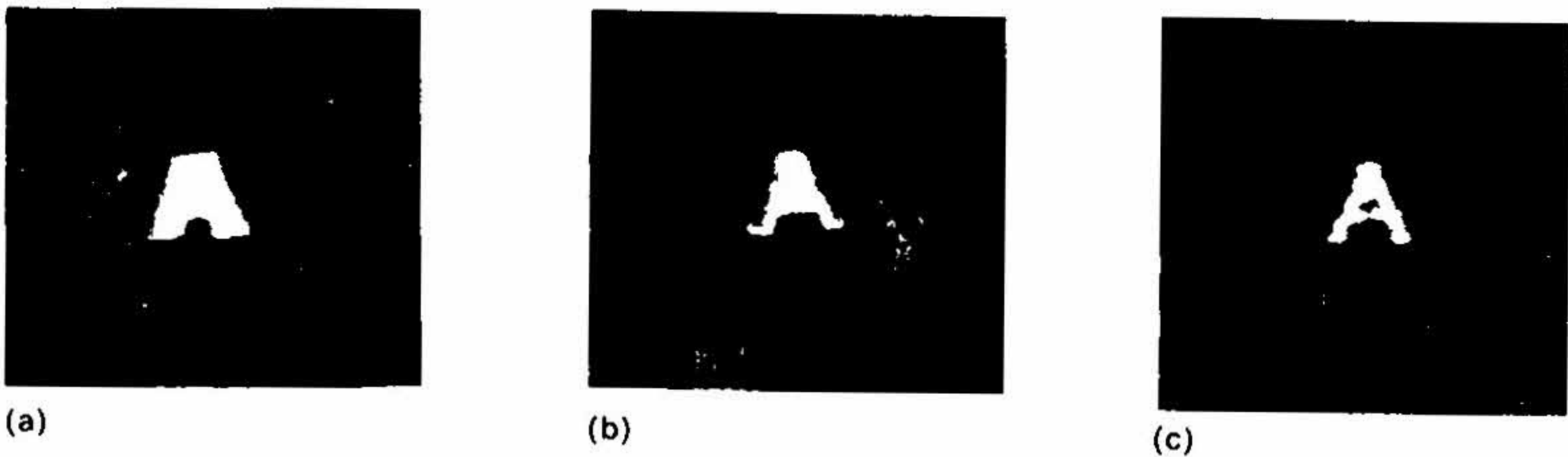


FIG. 4. (a) The test blurred object, (b) deblurred output with the filter in fig. 3(a) and (c) output with the Vasu-Rogers filter.

References

1. ANDREWS, H. C. AND HUNT, B. R. *Digital image restoration*, 1977, Prentice-Hall.
2. GOODMAN, J. W. Coherent image deblurring, in *Coherent optical engineering* (ed.) F T. Arecchi and V. Degiorgio, 1977, pp. 263-280, North-Holland.
3. DALLAS, W. J. Computer generated holograms, in *Computer in optical research* (ed.) B. R. Frieden, 1980, 41, pp. 291-366, Springer-Verlag.
4. VASU, R. M. *Coherent and noncoherent deblurring technique*, Ph.D. Thesis, 1980, Univ. of Aston, Birmingham, U.K.
5. HSUEH, C. K. AND SAWCHUK, A. A. Computer-generated double-phase holograms, *Appl. Opt.*, 1978, 17, 3874-3883.
6. VASU, R. M. AND ROGERS, G. L. Image deblurring with computer generated double-phase holograms, *Pattern Recognition*, 1981, 14, 297-303.

Thesis Abstract (M.Sc.(Engng))

Electrical breakdown characteristics of high-temperature gases under non-uniform field conditions by M. Joy Thomas.

Research supervisor: M. S. Naidu.

Department: High Voltage Engineering.

1. Introduction

Currently a trend is in vogue for an increase in the temperature rating of electrical machinery. This is applicable to high-voltage equipment also in which air or sulphurhexafluoride (SF_6) is used for insulation purposes. A gas when used as an insulating medium must be stable during the working conditions, *e.g.*, for busbar temperatures of 353-373° K (80-100°C) in compressed gas-insulated system (CGIS) equipment¹. Also a knowledge of the electrical breakdown of high-temperature gases is important to understand the physical processes occurring in high-voltage, high-power-circuit-breaker arcs².

In view of the above, investigations have been carried out to study the breakdown behaviour of SF_6 , nitrogen and air at temperatures from 23°C (296° K) to 200° C (473° K) over the gas-pressure

range 0.39 to 9.35 torr ($0.8 \times 10^{16} \leq N \leq 30.5 \times 10^{16} \text{ cm}^{-3}$) using a coaxial cylindrical electrode geometry of fixed gap spacing of 5 mm, in SF_6 , nitrogen and air. The gap separation was always constant at 5 mm.

2. Experimental techniques

In the measurement of electrical discharge parameters of gases at high temperatures it is necessary to maintain the temperature of the gas at a stable value. In the present study, a 'heatpipe' apparatus was used for the first time to measure the dc breakdown voltages at temperatures up to 200°C . A schematic diagram of the apparatus is shown in fig. 1 and is described in detail by Hemamalini *et al*³.

The experiments were conducted at different temperatures. At each temperature the breakdown voltages were measured and were observed to be within the inherent experimental error limits ($\pm 4\%$ at low Nd values which reduce to better than $\pm 0.5\%$ at high Nd values studied).

3. Results and discussion

The dc breakdown voltages obtained in the present study are shown in figs 2–5. The data are plotted as a function of Nd (product of gas number density and gap distance). During the course of the experiments, measurements were made at different pressures and the pressure values were converted into 'N' values taking temperature into consideration to obtain the Nd values shown in the figures.

3.1. Nitrogen

Values of V_b as a function of Nd in nitrogen are shown in fig. 2. The scatter in V_b when the temperature of the gas changed from 23 to 200°C is observed to be $\pm 5\%$ (maximum) at $\text{Nd} = 0.4 \times 10^{16} \text{ cm}^{-2}$ and $\pm 2.5\%$ at large Nd investigated. This scatter is larger than the experimental error limits ($\pm 4\%$ at $\text{Nd} = 0.4 \times 10^{16} \text{ cm}^{-2}$ and $\pm 0.5\%$ at $\text{Nd} = 15 \times 10^{16} \text{ cm}^{-2}$) described in the earlier section. This clearly shows that V_b varies with the temperature of the gas and hence it may be concluded that the Paschen's law fails in nitrogen at elevated temperatures as was also observed earlier⁴. The breakdown data are also in agreement with earlier measurements⁴, thus justifying the correctness of the experimental technique used.

Failure of Paschen's law in N_2 may be explained as due to the variation in secondary ionisation by positive ion bombardment of the electrode surfaces. For the electrode geometry studied (wire anode and cylinder cathode), the secondary electron emission yield is expected to be about two orders of magnitude higher because of the large cathode surface area. Also, with increasing temperature, the residual oxide layers on the electrode surfaces get progressively desorbed thereby causing increased electron emission. It was also observed that increasing the ambient temperature results in an increase in the dissociation rate of nitrogen ions⁵. Thus increased ion concentrations as a result of dissociation at higher temperatures can cause increased electron emission. These processes together appear to increase the secondary electron yield thus reducing the breakdown voltage of N_2 at elevated temperatures, thus invalidating the Paschen's law in this gas.

3.2. SF_6

Values of V_b as a function of Nd in SF_6 are shown in fig. 3. The same data are shown in fig. 4, in which the values of V_b are plotted as a function of temperature for different Nd values. It can be seen from fig. 3 that when the temperature of the gas was increased from 23 to 200°C , the scatter in V_b , increases with increasing Nd and reaches a maximum of about $\pm 20\%$ at the highest Nd value

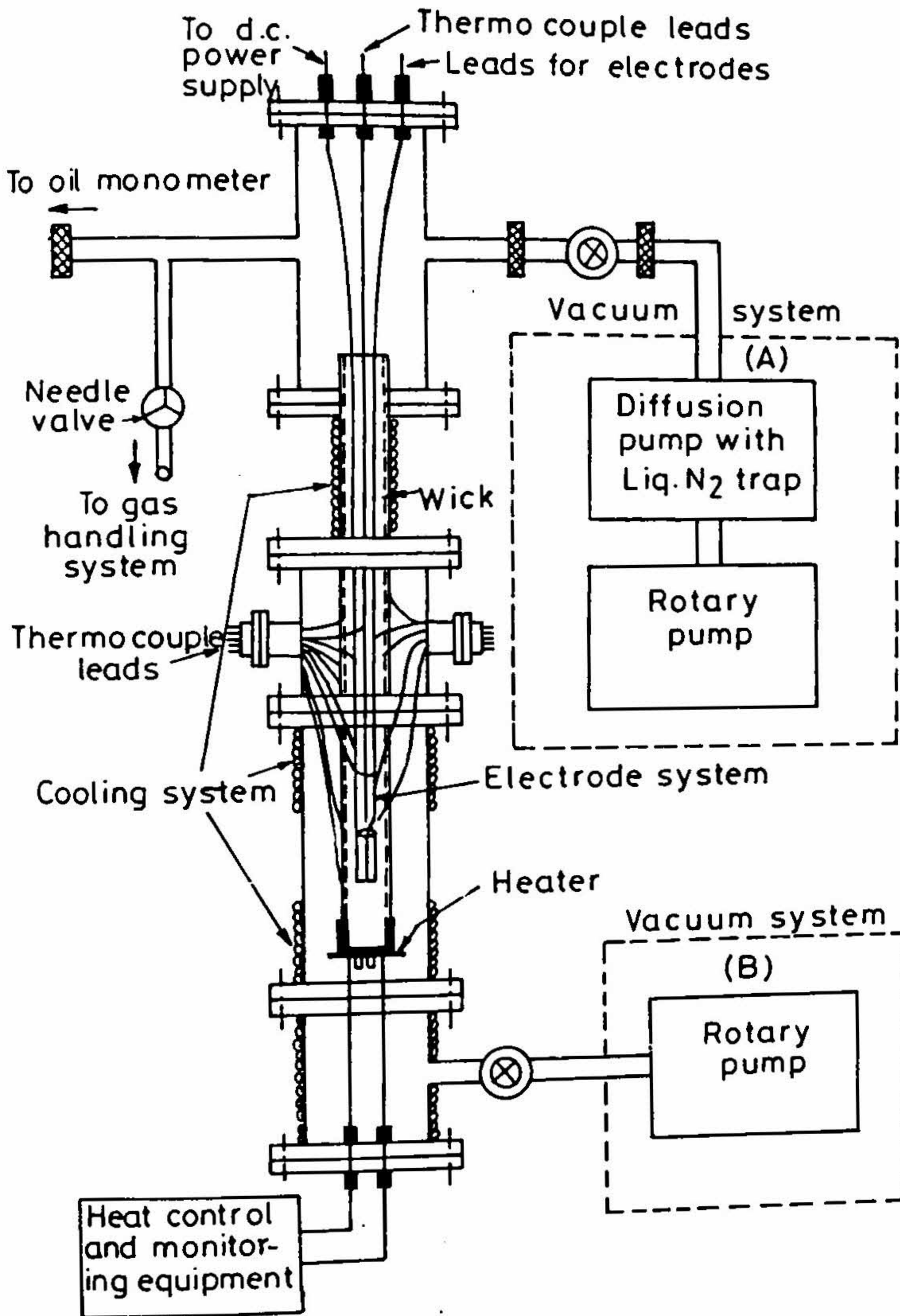


FIG. 1. Cross-section of the heat pipe.

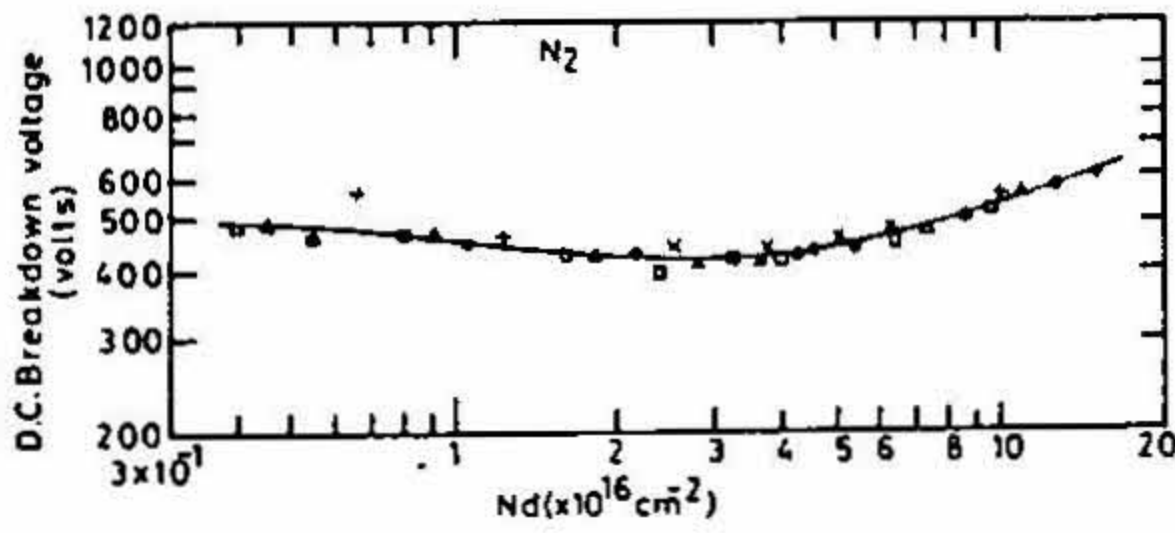


FIG. 2. dc breakdown voltage as a function of Nd at different temperatures in N_2 .

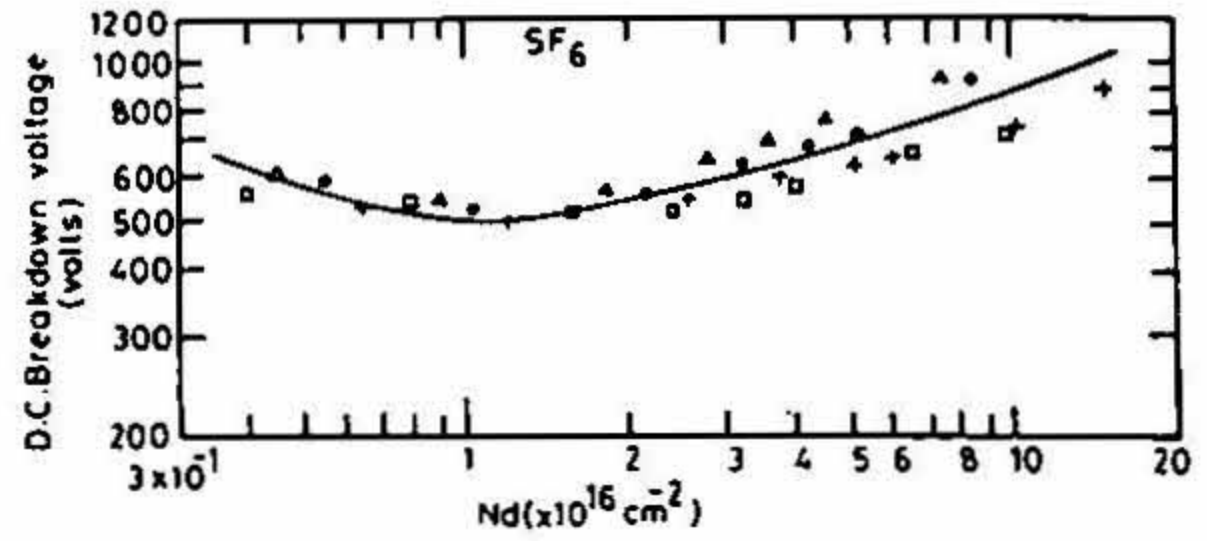


FIG. 3. dc breakdown voltage as a function of Nd at different temperatures in SF_6 . +:296°K; ●:353°K; △:413 K; □:473 K.

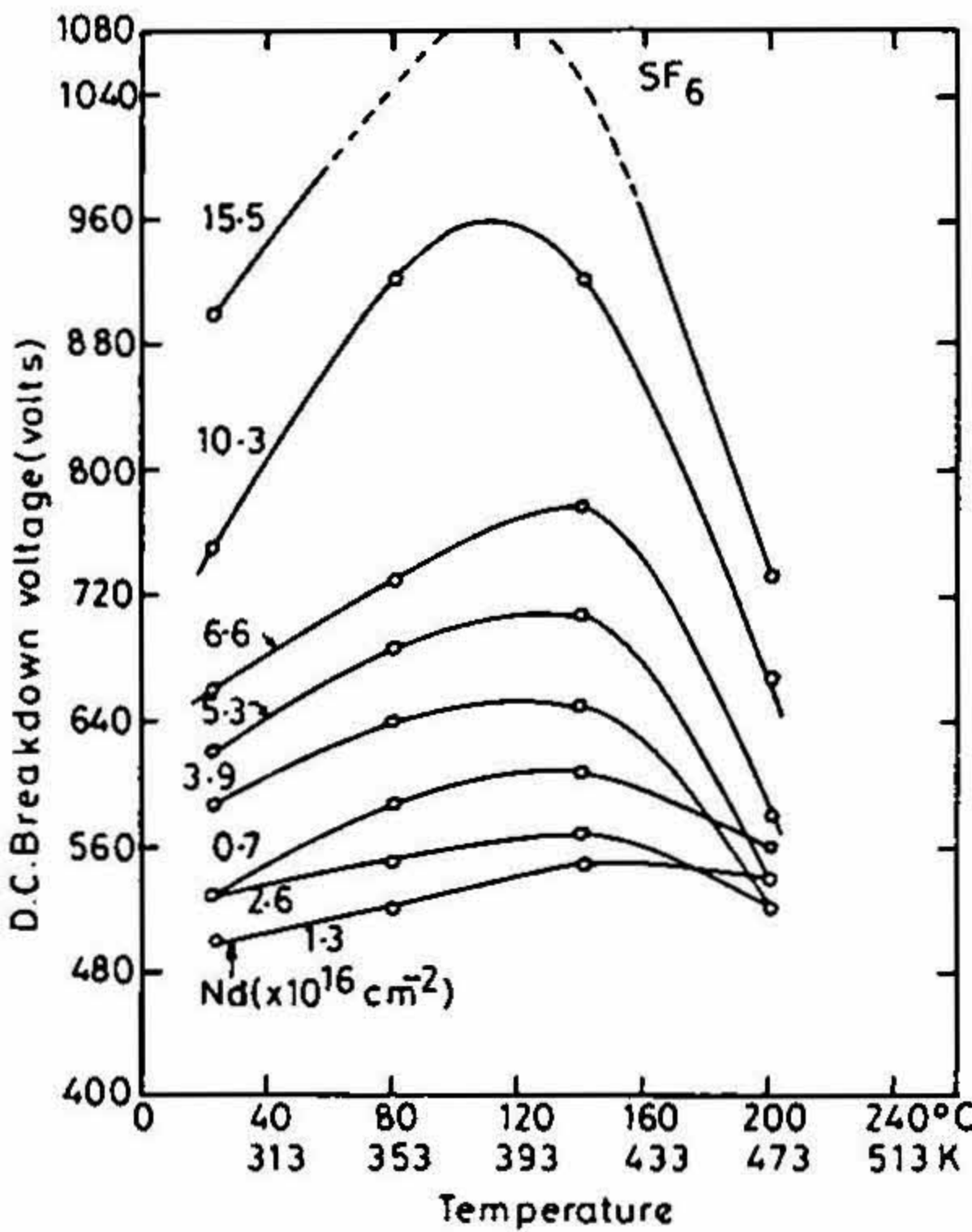


FIG. 4. dc breakdown voltage as a function of temperature at different Nd values in SF_6 .

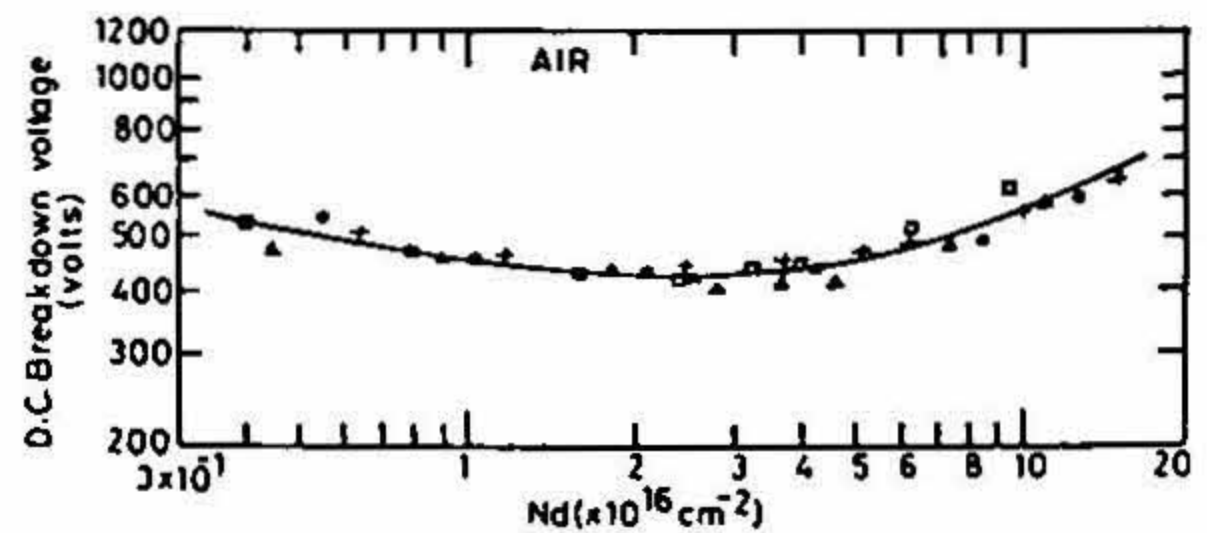


FIG. 5. dc breakdown voltage as a function of Nd at different temperatures in air. +:296 K; ●:353°K; △:413 K; □:473 K.

used in the study. These scatter values are larger than the inherent errors in the measurements which were discussed in the earlier section. It may be stressed that at any given temperature V_s showed no dependence on gas pressure and V_s were always consistent to within the experimental error limits. Thus, these large variations in V_s at elevated temperatures were observed to be real, clearly demonstrating the failure of Paschen's law in SF_6 at these temperatures. It can also be seen from fig. 4, that at any given value of Nd , V_s initially increases with temperature, reaches a maximum at about 140°C and then reduces.

The above phenomena of large scatter and the initial increase and reduction at higher temperatures of the breakdown data may be explained as due to the temperature dependence of: (a) secondary ionisation from electrode surfaces, (b) electron attachment, and (c) the detachment of electrons from

negative ions. The large scatter in V_s (up to $\pm 20\%$) may be explained as due to changes in surface conditions of the electrode surfaces in the presence of SF_6 gas. In addition to the residual oxide layers, the electrode surfaces get coated with thin layers of fluoride in the presence of SF_6 gas. In the present experimental arrangement the cylinder cathode area is quite large and in the presence of fluoride layer, the secondary electron yield becomes erratic, thus causing large variations in V_s . In addition, the electrons detached from negative ions generate positive ions, which on reaching the cathode, also contribute to secondary electrons. Since the electrode surface condition is not stable in the presence of SF_6 , the large variations in V_s are thought to be due to this phenomena. On the other hand, increase in V_s with temperature up to about 140°C can be due to the increased attachment rate (SF_6^- ions are formed in abundance over this temperature range). At still higher temperatures, the attachment rate reduces as was observed earlier⁶. This reduction in negative ion population results in decreased V_s at temperatures greater than 140°C (fig. 4).

3.3. Air

Values of V_s as a function of Nd were also obtained in dry air (fig. 5). The results show a variation of $\pm 7.5\%$ in V_s at high Nd values. These variations are clearly larger than the experimental error limits, thus clearly showing that the Paschen's law is not valid in dry air over the Nd values studied. These variations are due to the changing conditions of the electrode surfaces in the presence of oxygen. Increased oxidation of the electrode surfaces (especially in presence of a large cathode area as in the present electrode arrangement) with increasing temperature causes increased secondary electron yield thus resulting in reduced V_s as observed up to temperatures of about 100°C . At higher temperatures a slight increase in V_s was observed. This is possibly due to increased attachment rate in air at these higher temperatures.

References

1. CHRISTOPHOROU, L. G. *Gaseous dielectrics IV*, 1984, pp. 561-573, Pergamon.
2. LEE, T. H., GREENWOOD, A. N. AND WHITE, D. R. Electrical breakdown of high-temperature gases and its implications in post-arc phenomena in circuit breakers, *IEEE Trans.*, 1965, PAS-84, 1116-1125.
3. HEMAMALINI, N., LAKSHMINARASIMHA, C. S. AND NAIDU, M. S. Breakdown voltage and V-I characteristics of sodium vapour using coaxial cylindrical electrodes, *J. Phys. D. Appl. Phys.*, 1983, 16, 1489-1492.
4. HACKAM, R. Total secondary ionisation co-efficients and breakdown potentials of hydrogen, methane, ethylene, carbon monoxide, nitrogen, oxygen and carbondioxide between mild steel coaxial cylinders, *J. Phys. B Atom. Molec. Phys.*, 1969, 2, 216-233.
5. VARNEY, R. N. *Proc. 4th Int. Conf. on Ionisation Phenomena in Gases*, Uppsala, North-Holland, 1959, 1, 69-71.
6. HICKAM, W. M. AND BERG, D. Negative ion formation and electric breakdown in some halogenated gases', *J. Chem. Phys.*, 1958, 29, 517-523.

Thesis Abstract (M.Sc.(Engng))

Phase transformations in a Ti-7.9 at% Nb alloy by Anand W. Bhagwat.

Research supervisor: M. Mohan Rao.

Department: Metallurgy.

1. Introduction

The kinetics of diffusional growth of sideplates has been investigated in a number of ferrous and nonferrous systems¹⁻³. In all the investigations, the length of the longest plate and/or the thickness of the thickest plate seen on a plane of polish has been measured as a function of reaction time and temperature. These measurements have been taken to give the true length and thickness of the first nucleated plate in a three-dimensional ensemble of plates, and the growth kinetic laws have been determined. In the present investigation, a method is developed for obtaining the kinetic law from a measurement of the volume fraction and surface area per unit volume of the side plates using standard stereological techniques⁴.

2. Analytical method

Assume that the side plates have a rectangular shape. The analysis can be modified for other plate shapes by incorporating appropriate shape factors. Let $L(t, \tau)$, $W(t, \tau)$ and $\Delta(t, \tau)$ be the length, width and thickness of a plate at process time t , nucleated at time τ . The time dependence of these dimensions can be represented by the following general equations:

$$L(t, \tau) = a_L(t^n - \tau^n)^k \quad (1)$$

$$W(t, \tau) = a_W(t^m - \tau^m)^l \quad (2)$$

$$\Delta(t, \tau) = a_\Delta(t^p - \tau^p)^q \quad (3)$$

where a_L , a_W and a_Δ are determined by parameters such as diffusion coefficient, equilibrium concentrations, etc. and are time independent. The exponents p , m , n , k , l and q are determined by a specific growth model. Let the nucleation rate, $\dot{N}(\tau)$, be given by

$$\dot{N}(\tau) = b\tau^i \quad (4)$$

$i \geq 0$ represents, nucleation rate increasing with time, constant nucleation rate and nucleation rate decreasing with time, respectively. The volume fraction V_v , of the side plates is then given by

$$V_v = \int_0^t L(t, \tau) W(t, \tau) \Delta(t, \tau) \dot{N}(\tau) d\tau. \quad (5)$$

Substitution of equations (1) to (4) in (5) and simplification yields

$$V_v = U_1 L_M W_M \Delta_M N_v \quad (6)$$

where

$$U_1 = (1 + i) \int_0^1 (1 - u^n)^k (1 - u^m)^l (1 - u^p)^q u^i du \quad (7)$$

and is pure number. L_M , W_M , Δ_M are the length, width and thickness of the first nucleated plate at the process time t , and hence the largest characteristic dimensions of the plates in the collection of

plates at time t . N_v is the number of side plates per unit volume at time t . Similarly, one can write the surface area per unit volume of the plates, S_v .

$$S_v = 2U_2 L_M W_M N_v \quad (8)$$

where

$$U_2 = (1+i) \int_0^1 (1-u^n)^k (1-u^m)^l u^i du. \quad (9)$$

Equations (5) and (8) give

$$\Delta_M = (2V_v/S_v)/(U_2/U_1). \quad (10)$$

Thus, $(2V_v/S_v)$ is a measure of the true thickness of the thickest plate modified by the factor (U_2/U_1) . Let V_v° , S_v° and Δ_M° be the volume fraction, surface area per unit volume and the largest thickness at a particular time t_0 . One can then write

$$\frac{\Delta_M}{\Delta_M^\circ} = \frac{V_v S_v^\circ}{V_v^\circ S_v}. \quad (11)$$

This equation permits determination of the thickening kinetics from measured values of V_v and S_v .

Equation (6) for a rectangular plate can be modified to

$$V_v^2 = (U_1^2 \Delta_M^2 W_M^2 N_v^2) D_M^2 - (U_1^2 \Delta_M^2 N_v^2 W_M^4) \quad (12)$$

where D_M is the longest dimension in the collection of plates measured on a plane of polish.

Now, if a plot V_v^2 against D_M^2 is linear after a time t_0 and V_v also varies linearly with S_v , then one can conclude that:

- (1) the widening of the plate has stopped for $t > t_0$ and that $W(t) = W_M^\circ$;
- (2) the thickening has also stopped and that $\Delta(t) = \Delta_M^\circ$;
- (3) the value W_M° can be obtained from the measured slope and intercept in the graph relating V_v^2 to D_M^2 ; and
- (4) under these conditions $U_1 = U_2 = 1$ and the ratio $(2V_v/S_v)$ gives Δ_M° .

The above analysis does not assume any growth law for the lengthening. The growth law can now be determined by examining the relationship between the true length of the plate, $(D_M^2 - W_M^{\circ 2})^{1/2}$ and time.

3. Experimental programme

The Ti-7.9 at% Nb alloy used in this study was obtained from the Defence Metallurgical Research Laboratory, Hyderabad, in sheet form (1 mm thick). The composition was confirmed using X-ray fluorescent analysis and electron microprobe analysis. Specimens from this stock were heat treated in a two-zone vacuum furnace at different temperatures for varying periods of time. The specimens were examined using optical and electron metallographic techniques. The volume fraction and surface area of side plates was obtained using point counting methods and linear analysis.

4. Main results and conclusions

The linear relationship between volume fraction and surface area per unit volume at a reaction temperature of 650°C is shown in fig. 1. Similar results were obtained at different temperatures. The limiting thickness of the plates was obtained from these graphs at different temperatures. This did not significantly vary with temperature.

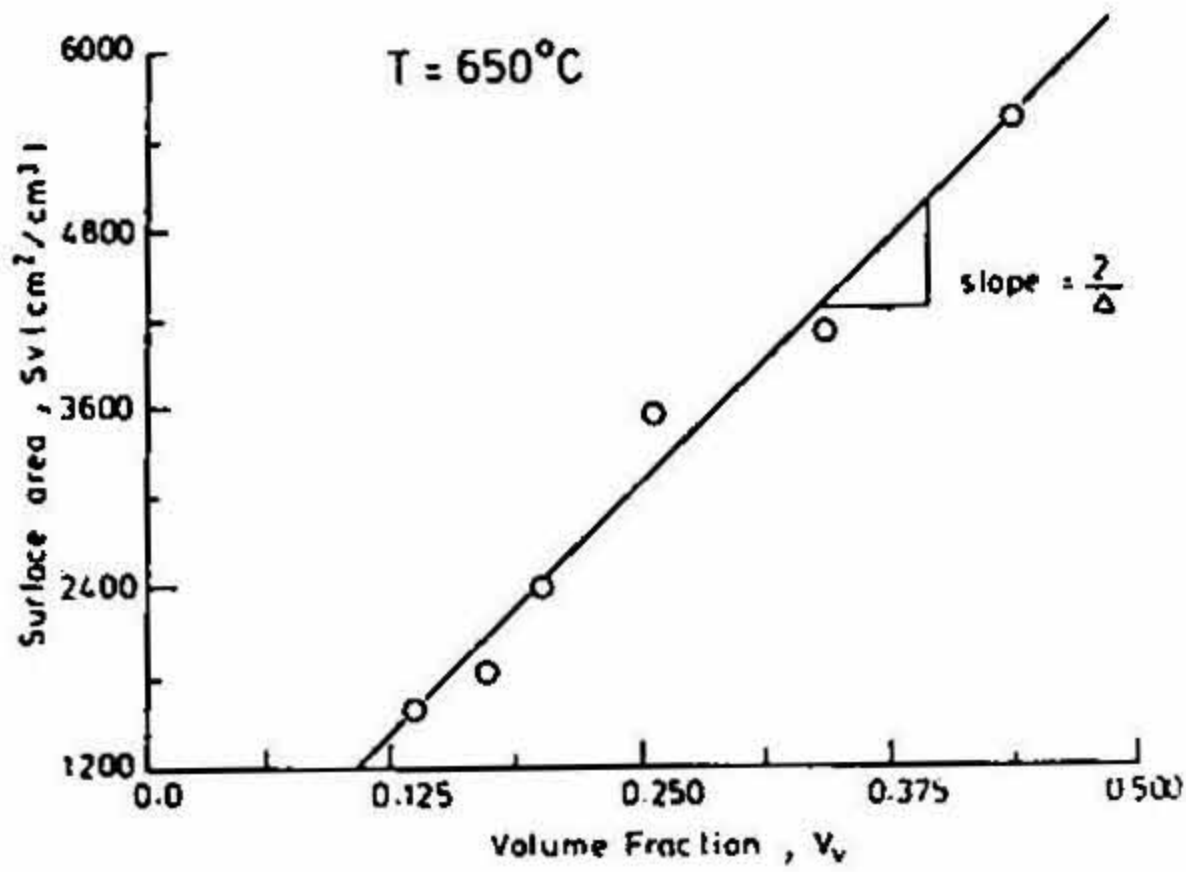


FIG. 1. Relationship between S_v and V_v for a sample treated at 650°C for different time durations.

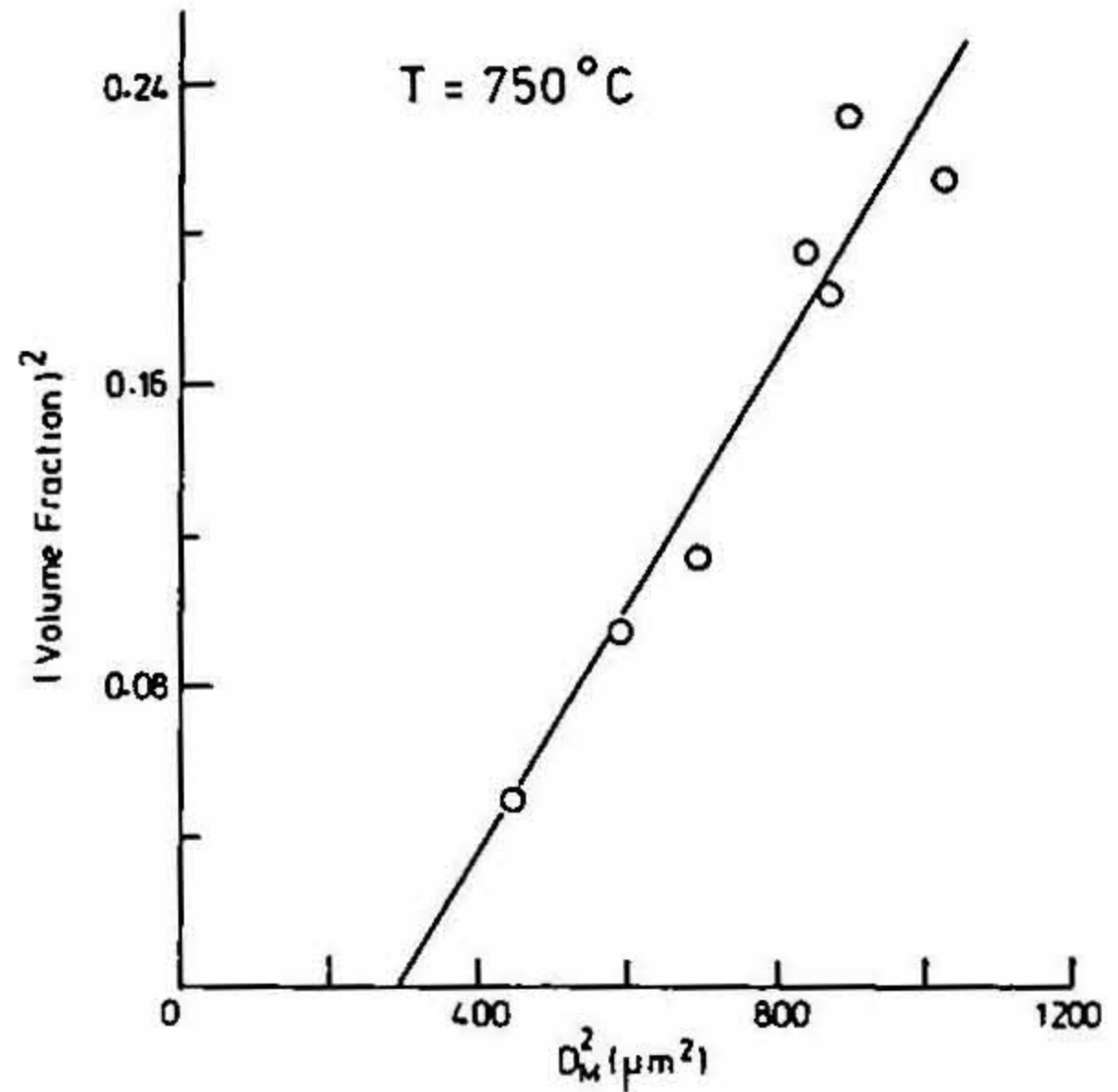


FIG. 2. Relationship between V_v^2 and D_M^2 for a sample treated at 750°C different time durations.

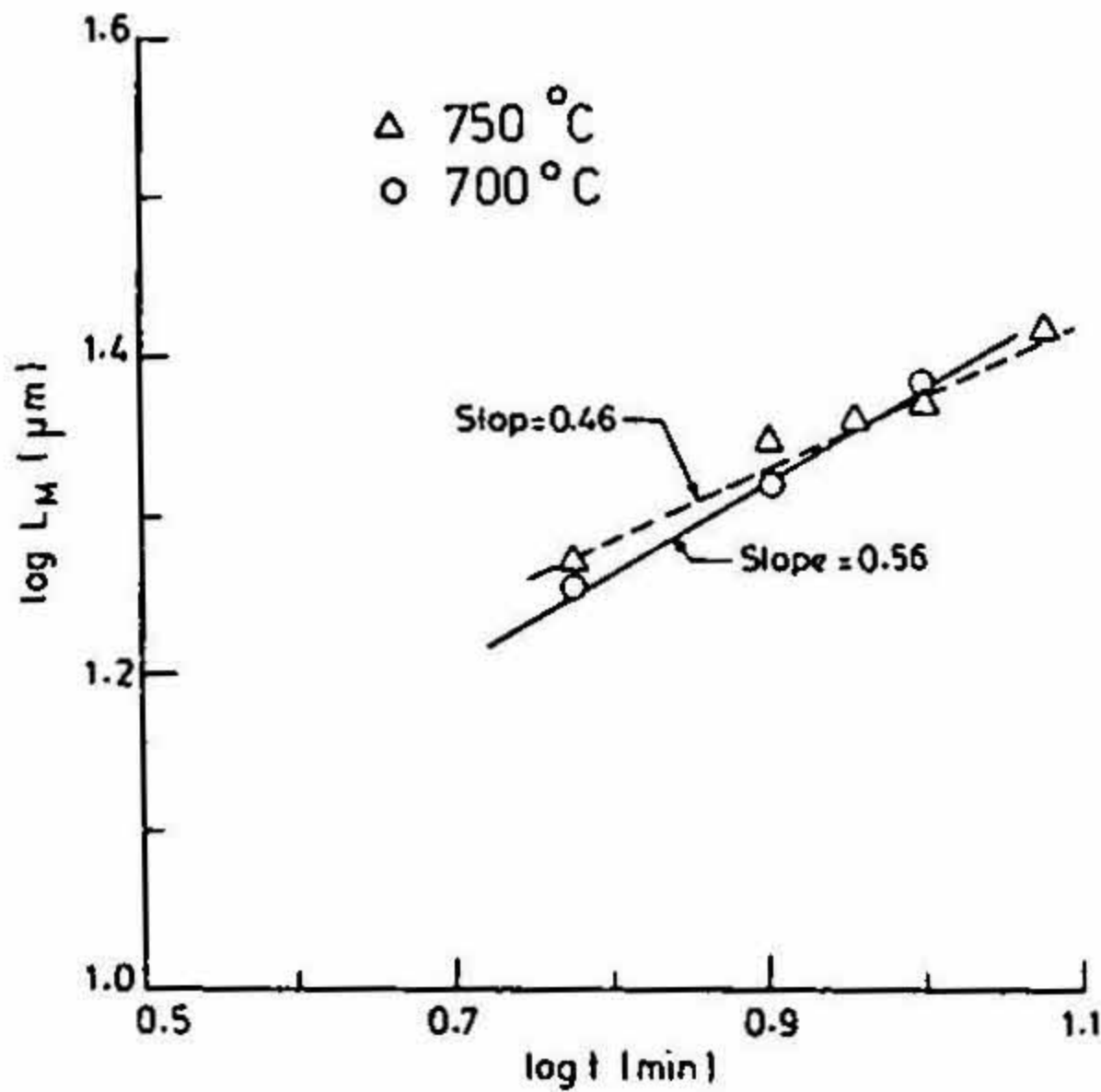


FIG. 3. Nonlinear relationship between L_M and t at 700°C and 750°C .

A typical curve relating V_v^2 to the square of the largest dimension measured D_M^2 is shown in fig. 2. This and similar graphs at different temperatures were used to obtain the limiting widths (W_M^0) of the plates as detailed in the analysis above.

The true length of the plates was calculated at each process time from the measured dimension D_M and the experimentally obtained values of W_M^0 . The results showed that the plates followed a parabolic growth law (fig. 3). Electron microscopic observations showed that both the broad faces

and edges of the plates consisted of an interface made up of ledges. A linear growth law was therefore to be expected. Our results clearly show that an interface made up of ledges, hence migrating by the ledge mechanism, can and do show a parabolic growth law. The reasons for this behaviour are not clear and need further investigation.

References

1. LAIRD, C. AND AARONSON, H. I. The growth of γ -plates in an Al-15% Ag alloy, *Acta Met.*, 1969, 17, 505-519.
2. SIMONEN, E. P., AARONSON, H. I. Lengthening kinetics of ferrite and bainite side plates, *Met. Trans.*, 1973, 4, 1239-1245.
3. SANKARAN, R. AND LAIRD, C. Kinetics of growth of platelike precipitates, *Acta Met.*, 1974, 22, 957-970.
4. DEHOFF, R. T. AND RHINES, F. N. *Quantitative microscopy*, 1968, McGraw-Hill.

Thesis Abstract (M.Sc.(Engng))

Static and dynamic analysis of curved members by A. R. Gopalakrishnan.

Research supervisor: S. Anantha Ramu.

Department: Civil Engineering.

1. Introduction

The thesis deals with the elastic analysis of a curvi-linear member. A computer software based on three-D analysis is developed and the complete program is described. The program can handle several shapes of cross-section and different types of loadings such as gravity, concentrated loads and uniformly distributed surface loadings. The program contains pre- and post-processor capabilities, and can be operated on PCs, mini and mainframe computers.

2. Scope

The thesis is organised in six chapters. Chapters I and II contain introduction and literature survey. Though extensive work is reported on curved members, finite-element modelling of such member as considering them as three-D isoparametric, eight- and 20-noded brick elements does not seem to be reported. With this in view the problem was tackled and a software operational on both PCs and main computers is developed.

The finite-element method of analysis and the software developed are described in Chapters III and IV. Chapter V presents numerical results and Chapter VI concluding remarks.

3. Results and conclusions

The three-D brick element developed in the software is of two types. They are eight- and 20-noded isoparametric brick elements. The results from the proposed program are compared extensively with the elementary solutions³ for straight and curved members available in the literature. The comparison is found to be within permissible limits of accuracy. Results obtained using different three-D finite element meshes are reported in the thesis.

The program can also handle three-D dynamic analysis of straight and curved members. An example of reinforced concrete corbel subjected to sudden application of load from gantry girders is solved⁴. Both free and forced vibration time history responses are given in the thesis. For free vibration analysis both Jacobi and subspace iteration methods⁵ are employed and compared. It is found that subspace iteration is closer to exact solution.

The efficiency of the program in terms of CPU time disk and core storage are found to be very encouraging compared to general purpose program like SAP IV. The present program employs incore solution (active column profile method) for solving the system of simultaneous equations which forms a major part of the program and does not make use of disk storage space for the creation of intermediate files like SAP IV. On account of this the solution procedure is found to be extremely fast by the present program. For example, to solve a system of 980 equations using eight-noded brick- and finite-element mesh of $10 \times 6 \times 4$ totalling 240 elements and 385 nodes, it was found that the present program required seven minutes of CPU time and 116,501 words of central memory, while SAP IV required 18 minutes and 15 sec. Further, because SAP IV is not so much in core as compared to the proposed program, the former required nearly 6,000 blocks of disk storage for the above problem. The present program took a connect time of seven minutes, which was the same as the CPU time to solve the above problem, while SAP IV took 1 hour as it involved large I/O disk operations. The above comparison was carried out on a VAX 11/730 computer. Thus, the program developed will have useful applications for the three-D finite-element analysis.

References

1. TIMOSHENKO, S. AND GOODIER, T. N. *Theory of elasticity*, McGraw-Hill, 1951.
2. ZIENKIEWICZ, O. C. *The finite element method in engineering sciences*, McGraw-Hill, 1971.
3. SEELY, F. B. AND SMITH, J. O. *Advanced mechanics of materials*, Wiley, 1957.
4. BIGGS, J. M. *Introduction to structural dynamics*, McGraw-Hill, 1964.
5. BATHE AND WILSON, E. L. *Numerical methods in finite element analysis*, Prentice-Hall, 1976.